This manuscript has been submitted for publication in JOURNAL OF PETROLOGY. Please note that, despite having undergone one round of peer-review, the manuscript has yet to be formally accepted for publication (corrections recently returned to journal). Subsequent versions of this manuscript may have slightly different content. If accepted, the final version of this manuscript will be available via the 'Peer-reviewed Publication DOI' link on the right-hand side of this webpage. Please feel free to contact the authors; we welcome feedback.

Figures are at the end of this document.

A new calibration of the OPAM thermobarometer for anhydrous and hydrous mafic systems

Oliver Higgins[1]*, Michael J. Stock[1]

[1] Discipline of Geology, School of Natural Sciences, Trinity College Dublin, Dublin 2, Ireland

*Corresponding author (olhiggin@tcd.ie; ORCID iD: 0000-0001-9960-934X)

ABSTRACT

Melt-based thermobarometers are essential tools to recover pre-eruptive magma storage conditions through their application to bulk rock and liquid chemistry. In active volcanic systems, thermobarometric results can be combined with independent geophysical data during or after an eruption to validate conceptual models. In this contribution, we revisit the thermobarometer for melts equilibrated with the mineral assemblage of olivine + plagioclase + augitic clinopyroxene (OPAM). We first demonstrate that the most widely applied OPAM thermobarometer suffers from both random and systematic uncertainty even for anhydrous melts, and that the uncertainty increases proportionally with melt H_2O. To address this issue, we use a modern compilation of anhydrous and hydrous OPAM-saturated experiments to regress a new melt-based OPAM thermometer and barometer. Our new equations recover a validation dataset with a standard error estimate (SEE) of ±1.1 kbar and ±35 ˚C for pressure and temperature respectively, as well as a low systematic uncertainty that does not depend on melt H_2O. Additionally, we present a novel statistical approach to determine the probability that a given melt is OPAM-saturated, which can be used alongside petrographic observations. Our thermobarometer and saturation test are presented as a straightforward R script which reads from an input csv file to be populated with natural data. We benchmark the new calibrations on the products of the 2015 eruption of Wolf Volcano (Isabela Island, Galápagos) and the 2014-2015 Holuhraun eruption (Iceland), both of which have independent geophysical estimates of magma storage that agree well with our thermobarometric results.

KEYWORDS

Multiple saturation; OPAM; thermobarometry; basalt; Galápagos; Iceland

INTRODUCTION

Thermobarometry, the retrieval of pressure (P) and temperature (T) information from magmas, provides a quantitative window into the physicochemical structure of magmatic systems (Blundy and Cashman, 2008; Grove et al., 1992; Neave and Putirka, 2017; Putirka, 2008). Thermobarometric equations relate T (˚C) and P (kbar) to the measured composition (X) of a melt and/or mineral(s) using equilibrium crystallisation experiments (Putirka, 2008). Equations may have a general form grounded firmly in thermodynamics with additional empirical terms to improve the goodness of fit (e.g., Masotta et al., 2013; Neave and Putirka, 2017; Putirka, 2016), or be purely empirical and consist only of compositional variables with or without P and T terms as independent variables (e.g., Jorgenson et al., 2022; Ridolfi and Renzulli, 2012). Irrespective of the calibration strategy, thermobarometers have significant scope as petrological volcano monitoring tools. For example, P data can independently validate geophysical estimates of pre-eruptive magma storage depth during or after eruptions (Hartley et al., 2018; Stock et al., 2018; Ubide et al., 2023) or catalogue past changes in magma P and T for eruptions of volcanoes that lack a protracted historical monitoring record (Bouvet de Maisonneuve et al., 2021; Higgins et al., 2021a; Jorgenson et al., 2024; Weber et al., 2020). Therefore, access to accurate, precise, and readily applicable thermobarometers is an essential component of volcanic hazard management and eruption forecasting.

Melt-based thermobarometers (e.g., Blundy, 2022; Grove et al., 1992; Helz and Thornber, 1987; Wilke et al., 2017; Yang et al., 1996) are a particularly useful implementation of the method as P-T estimates can be derived from the chemistry of a single phase which is often easily recovered from matrix glass, melt inclusions, or whole-rock data. However, to be reliably applied, the input melt composition must represent a true equilibrium liquid, free from the effects of magma mixing or crystal accumulation which are rife in magmatic systems (Cashman and Blundy, 2013; Kent et al., 2010; Passmore et al., 2012). Melt-based thermobarometry equations regress melt composition against P or T by assuming that the melt

is buffered by a discrete, low-variance phase assemblage; the mineral proportions change in response to *P*, *T*, and bulk composition, imparting a predictable chemical control on the coexisting melt. Such "multiple saturation thermobarometers" are broadly applicable in both high-melt-fraction and low-melt-fraction magmatic systems, recording *P*-*T* conditions at the point where melts decouple (via eruption or melt migration) at a speed that is too rapid for further chemical equilibration with the buffering crystal assemblage (Solano et al., 2014; Jackson et al., 2018; Lissenberg et al., 2019; Blundy, 2022).

The OPAM thermobarometer is a melt-based multiple-saturation thermobarometer relying on equilibrium between the mineral assemblage olivine + plagioclase + augitic clinopyroxene (the olivine gabbro cotectic; Herzberg, 2004). Early work showed that the location of the OPAM cotectic was strongly *P* dependent, and could be parameterised as a function of melt major element composition (Ca+Mg+Al+Si+Fe+Na; Shi, 1993, 1992). Later, the effect of minor elements (K, Ti, Cr) were deemed significant to capture the melt composition effect within the form of the cotectic equation (Grove et al., 1992; Voigt et al., 2017; Yang et al., 1996). The Yang et al (1996) equations remain the most widely applied calibration of the OPAM cotectic (e.g., Baxter et al., 2023; Bell et al., 2021; Hartley et al., 2018; Stock et al., 2018); this model comprises three empirical equations which regress the molar proportion of three melt-compositional cations (Al, Ca, Mg) as separate functions of Na, K, Fe, Ti, Si, and *P* (kbar). Originally, these *P*-dependent equations were developed as a method to model basaltic fractional crystallisation and were not strictly proffered as a barometer (Yang et al., 1996). The calibration experiments were predominantly performed at 1 atmosphere (1 atm; n=164) and extrapolated across a range of crustal magma storage conditions (>1 atm to 10 kbar) using only a small number of high-*P* experiments (n=26). The hydrous, high-*P* experiments used to calibrate the Yang et al (1996) equations span up to ~2 wt.% H_2O (Baker and Eggler, 1987), theoretically limiting their applicability to low-H_2O ocean

93 island and mid-ocean ridge settings. However, the explicit effect of H_2O was not tested, even
94 though OPAM-saturated ($OPAM_{SAT}$) melts are stable across a wide range of melt H_2O content
95 (0-7.7 wt% H_2O; Fig. 1a), with increasing H_2O supressing the *T* and MgO (wt%) of OPAM
96 saturation (Fig. 1b). In general, constraining the effect of H_2O on thermobarometric models is
97 vital given that the addition of even moderate concentrations (much less than 2 wt%) to
98 anhydrous compositions can have a drastic effect on phase equilibria in basaltic systems
99 (Almeev et al., 2012, 2007; Husen et al., 2016). Yang et al., (1996) also presented a separate
100 thermometric equation that regressed *T* (˚C) as a function of the same melt composition
101 variables (Na, K, Fe, Ti, Si) plus *P* as an independent variable. The quoted uncertainty of the
102 Yang et al (1996) thermometer is ±20 ˚C, based on the observation that 170 of the 190 calibrant
103 experiments are recovered with a T residual of ±20 ˚C or less. However, this assessment of
104 uncertainty was self-validated by Yang et al (1996), calculated with the calibration
105 experimental dataset rather than an independent set of experiments.
106 Hartley et al., (2018) first implemented the three Yang et al (1996) *P*-dependent
107 compositional equations as a cohesive barometer, returning the *P* that minimised the χ^2 misfit
108 between measured Al, Ca, and Mg content and those predicted by the three equations. The
109 Yang et al (1996) equations were solved at 0.01 kbar intervals between -5 and 15 kbar until the
110 misfit χ^2 was minimised, indicating the unique *P* of convergence. The misfit χ^2 is defined by
111 the general equation:
112
113 $$\chi^2 = \sum_{i=1}^{3} \left(\frac{X_i - Y_i}{\sigma_i} \right)^2 \quad (1)$$
114
115 where X_i are the measured cation fractions of Al, Ca, and Mg, Y_i are the cation fractions
116 predicted from the three Yang et al (1996) equations, and σ_i is a term for analytical uncertainty

that allows some leeway in the convergence. As well as providing the *P* that minimised the misfit χ^2, Equation 1 also returns a measure of the convergence quality or probability of fit (P_F). Hartley et al (2018) repurposed this quantitative information as a probability that the melt was $OPAM_{SAT}$, using it to screen natural melts that would not yield a reliable *P* of three-phase saturation. A low P_F indicates that the three Yang et al (1996) equations do not intersect closely in multidimensional space outside of analytical uncertainty and so there is no unique *P* solution for the input melt. Hartley et al (2018) suggested setting a cut off for P_F at <0.8, which was determined by observing the P_F above which the *P* of an experimental dataset was reproduced with low random and systematic uncertainty by the Yang et al (1996) equations, applied through Equation 1. Their test dataset contained 157 $OPAM_{SAT}$ experiments including some of those used to calibrate the Yang et al (1996) equations as well as several more recent studies. Hartley et al (2018) found that the systematic (+1 kbar) and random (±2.5 kbar) uncertainties when using the whole dataset dropped after removing around 40% of the $OPAM_{SAT}$ experiments, which all had P_F <0.8, yielding new lower systematic (+0.34 kbar) and random (±1.32 kbar) uncertainties for the P_F-filtered dataset. However, by using experiments from the Yang et al (1996) equations in their test dataset, the model performance was, again, partially self-validated by Hartley et al (2018). Further, the removal of around 40% $OPAM_{SAT}$ experiments raises questions about the reliability of their quoted ±1.32 kbar barometer uncertainty if no methodological or analytical reason for their omission can be found.

Baxter et al., (2023) released a Python-based implementation of Equation 1, mimicking the approach of Hartley et al (2018). Their code provides an open-access, reproducible method to recover *P* estimates and P_F for $OPAM_{SAT}$ natural melts via the three Yang et al (1996) cotectic equations. The Yang et al (1996) *P*-dependent thermometer was omitted from their code. Baxter et al., (2023) tested the Hartley et al (2018) method using a near identical workflow, collecting a dataset which included Yang et al (1996) calibrant experiments plus a

suite of newer studies (n=250). Using a filter of $P_F \geq 0.8$, they found that only 92 experiments remained (37%) which had been reproduced with a mean absolute error of ±1.13 kbar. The Baxter et al., (2023) test of the Hartley et al (2018) method contains the same issues of self-validation and unexplained filtering of $OPAM_{SAT}$ experiments which remain to be justified.

The Yang et al (1996) cotectic equations have also featured in other implementations of the melt-based OPAM thermobarometer. Michael and Cornell (1998) rearranged the Ca Yang et al (1996) equation for *P* and used it as a stand-alone barometer; rearranging multiple linear regressions in this way is mathematically incorrect (Hartley et al., 2018). Voigt et al (2017) presented an updated parameterization of the three *P*-dependent Yang et al (1996) equations by considering Cr, Fe^{2+} and Fe^{3+} as additional variables, although there is no reproducible method with which to apply and test their equations (e.g., Baxter et al., 2023). Kelley and Barton (2008) calculated the liquid compositions at 0.1 kbar increments with the three Yang et al (1996) cotectic equations, converted them to normative mineral compositions, regressed *P* against the calculated and original compositions, and finally computed the mean *P*. This unduly complex method performs significantly worse than the original Yang et al (1996) barometer applied via the approach of Hartley et al (2018) when tested using $OPAM_{SAT}$ experiments (Baxter et al., 2023).

In this contribution, we re-visit the OPAM thermobarometer using the wealth of new experimental data available since the implementation of Yang et al (1996). An experimental dataset of $OPAM_{SAT}$ experiments with no obvious quality issues are compiled. These experiments span 0-7.7 wt% H_2O and 0.5-10 kbar, encompassing the full crustal spectrum of $OPAM_{SAT}$ melts. By first omitting studies which were used to calibrate the Yang et al (1996) equations, we test the robustness of the filtering method of Hartley et al (2018) and the quoted Yang et al (1996) *P* uncertainty (±1.13 kbar) of Baxter et al., (2023) using a truly independent test dataset. Based on these findings, we highlight the large true uncertainty associated with

the Yang et al (1996) thermometer and barometer, exacerbated by increasing melt H_2O. In light of this, we present a new empirical thermometer and barometer for $OPAM_{SAT}$ melts at anhydrous-hydrous conditions and crustal pressures (0.5-10 kbar) as a function of melt composition. We also introduce a new statistical method for determining the probability that a melt is OPAM saturated which allows for application of our geothermobarometer to natural melts where petrological constraints on multiple saturation are unavailable. Our equations are applied to basaltic erupted products from the 2015 eruption of Wolf Volcano (Isabela Island, Galápagos archipelago) and the 2014-2015 Holuhraun eruption (Iceland) which both have extensive petrographic, geochemical, and geophysical records (Halldórsson et al., 2018; Hartley et al., 2018; Stock et al., 2020, 2018).

METHODS

Database Assembly and Filtering

$OPAM_{SAT}$ experiments were collected from the Library of Experimental Phase Relations (LEPR; Hirschmann et al., 2008), corrected for typos and copy errors, and supplemented with experiments published after circa 2008. Experiments conducted at 1 atm were excluded to avoid issues of rapid disequilibrium crystal growth in 1 atm experiments (Mollo et al., 2010; Ziberna et al., 2017) and to prevent an overweighted regression at pressures (depths) irrelevant to pre-eruptive magma storage (Neave and Putirka, 2017). Any studies not reporting the abundances of mineral run products were not considered further. The upper *P* was limited to 10 kbar where $OPAM_{SAT}$ data become sparse, resulting in extrapolation over large *P* intervals. Ten kbar (~32 km in oceanic crust; Putirka, 1997) encapsulates the thickness of most oceanic crust and is the *P* limit of the thermobarometer calibration of Yang et al (1996). No filter was used for melt H_2O as the pre-existing H_2O content of a magma is rarely known

192 which would limit the confident application of our updated equations. Experiments
193 crystallising major silicate phases outside of OPAM (biotite, amphibole, orthopyroxene,
194 garnet) were removed. However, we retained experiments which crystallised Fe-oxide phases,
195 despite Putirka (2008) finding that strictly $OPAM_{SAT}$ experiments (i.e., without Fe-oxides) led
196 to an improved fit, as removing these experiments may also limit the model applicability in
197 natural systems. Removing experiments crystallising major silicate phases outside of OPAM
198 is important as the critical assumption of an OPAM thermobarometer is that the melt is buffered
199 by a common assemblage of olivine + plagioclase + augitic clinopyroxene whose compositions
200 and proportions change as a function of *P* and *T*. A total alkali filter was not initially applied,
201 although we discuss the role of alkalis later; while Hartley et al (2018) state that the OPAM
202 thermobarometer should be avoided for transitional or alkali basalts due to poor performance,
203 this is at odds with the Yang et al (1996) equations which are calibrated using some alkalic
204 melt compositions. Indeed, our compiled $OPAM_{SAT}$ experiments span to alkalic melt
205 compositions (Fig. 1c).

206 The liquid cation fractions of experimental melts were calculated using the method
207 outlined in Table 1 of Putirka (2008), and are denoted by X followed by the oxide subscript
208 (e.g.,$X_{AlO_{1.5}}$). Additional experiments were removed which did not report $X_{KO_{0.5}}$ (i.e., where it
209 is not clear whether potassium is legitimately absent or not reported; 29 experiments) and/or
210 which exhibited iron loss or gain greater than 20% (7 experiments). Outliers, defined as an
211 abnormal value at odds with the regular distribution of the dataset, were subsequently appraised
212 in the remaining data by inspecting x-y plots of liquid cation fractions. The potential for outliers
213 is high due to the difficulty of performing and analysing experimental run products. However,
214 the dataset appeared largely coherent, and few outliers were identified. The exception was
215 scatter at high and low X_{CaO}, which was removed using a filter of $0.04 < X_{CaO} < 0.14$ (n=12),
216 and a single experiment (Y0206-1) from Neave et al (2019) which showed anomalously

heterogeneous glass compositions. Our final $OPAM_{SAT}$ compilation (n = 249) is reported in Supplementary Table 1a, including the mean and range of key variables (Supplementary Table 1b). A full reference list for all experiments can be found in Supplementary Table 1c. To our knowledge, this dataset consists of good-quality $OPAM_{SAT}$ experiments for calibrating or testing OPAM thermobarometers. However, to address our earlier comment on the limitation of the Baxter et al., (2023) and Hartley et al (2018) studies, we subset our $OPAM_{SAT}$ compilation (n=249) to remove all calibrant experimental studies named in Table 4 of Yang et al (1996) when testing the performance of the Yang et al (1996) barometer and thermometer (n=199; marked in Supplementary Table 1a).

Asserting OPAM saturation

Determining OPAM saturation is critical for reliable application of the thermobarometric equations which rely on this equilibrium assemblage. We stress that the most valid method for determining multiple saturation is to use petrographic indicators such as texturally equilibrated OPAM mineral phases (i.e., euhedral, not resorbed). For bulk rock analyses of magmas considered as putative melts, "petrological cannibalism" (Cashman and Blundy, 2013) may make quantitative textural analysis (e.g., crystal size distributions) and/or chemical mapping essential to elucidate exogenous OPAM crystal populations (Higgins et al., 2021b; Neave et al., 2017, 2014; Sheldrake and Higgins, 2021). For example, a hallmark of less-evolved basaltic magmas is high-An# phenocrysts, or phenocryst cores, at disequilibrium with their matrix glass (Neave and Namur, 2022). Significant crystal accumulation may be identified by strong correlations between modal mineral abundances and mineral-compatible trace elements, although it can also be necessary to identify and correct for an accumulated mush liquid in addition (Passmore et al., 2012). Magmas which have accumulated crystals should have their bulk chemistry corrected by mass balance, akin to a post-entrapment

crystallisation correction for melt inclusions, before using any melt-based thermobarometer. Finally, we note that the petrographic absence of a phase in hand sample does not preclude its presence in the crystallising assemblage. This is often termed "cryptic fractionation" and manifests itself in mid-ocean ridge basalts as the "pyroxene paradox" whereby the chemical mass balance between minerals, glass, and whole rock requires clinopyroxene that is conspicuously lacking as a phenocryst (Dungan and Rhodes, 1978; Grove et al., 1992; Herzberg, 2004; Kelley and Barton, 2008; Lissenberg et al., 2019). Based on the range of processes which may prevent a magma from representing an $OPAM_{SAT}$ melt, it is preferable to use clean, unaltered, microlite-free glass compositions in petrographically characterised magmas as the input for OPAM thermobarometry.

An alternative, or a complement, to petrographic analysis is a melt-based binary classifier to distinguish $OPAM_{SAT}$ melts from OPAM undersaturated ($OPAM_{UNSAT}$) melts. A classifier is particularly useful for processing large regional or global datasets where original samples cannot be obtained, or whole rock data where multiple saturation cannot be petrographically determined. Previous methods include graphical (Maclennan et al., 2001; Yang et al., 1996), empirical (Kelley and Barton, 2008), and statistical or probabilistic (Baxter et al., 2023; Hartley et al., 2018) approaches. The latter remains the most widely applied but suffers from false negatives whereby $OPAM_{SAT}$ experimental melts with no explainable defect are classified as $OPAM_{UNSAT}$ melts (Baxter et al., 2023; Hartley et al., 2018). A saturation classifier must work to limit, as much as feasibly possible, the presence of false positives (false report of $OPAM_{SAT}$ melts) or false negatives. The aim of an OPAM saturation binary classifier, or any binary classifier for that matter, is to identify or engineer differences between the two categories of data so they can be mathematically discriminated from one another. We have developed a simplified statistical approach, presented as an R script (R Core Team, 2023),

266 which returns a probability of OPAM saturation (P_{SAT}) using our up-to-date experimental
267 dataset.

268 We first consider a set of critical oxides which must be reported and non-zero (i.e.,
269 chemically measured in either an experimental or natural melt) to use our saturation test. The
270 critical oxides are chosen by inspecting our $OPAM_{SAT}$ compilation and are expressed in wt%
271 in their raw form: SiO_2, Al_2O_3, MgO, FeO, CaO, Na_2O, K_2O, TiO_2. For the entire saturation
272 test process, all experimental and natural melts are normalised to 100 wt% anhydrous
273 considering just these eight critical oxides. The eight critical oxides also perform an essential,
274 non-negotiable, first-pass test for identifying $OPAM_{SAT}$ melts, by using them to define a series
275 of OPAM convex hulls. A convex hull is a polygon that connects the outer ring of points in an
276 X-Y plot, in this case a Harker plot of two critical oxides (e.g., SiO_2[x] versus Al_2O_3[y]; Fig.
277 2a). The OPAM convex hull is expanded to account for an average relative analytical
278 uncertainty of ±5%. We define the OPAM convex hull for the 28 pairwise combination of the
279 8 critical oxides and use it as an initial test to verify if a natural or experimental melt of
280 unknown saturation state could be $OPAM_{SAT}$. In other words, if a melt subjected to the
281 saturation test does not fall inside all 28 OPAM convex hulls, the melt does not represent a
282 reasonable approximation of an $OPAM_{SAT}$ melt in multi-dimensional space based on our
283 current experimental knowledge. The OPAM convex hull test provides a rapid method to
284 preliminarily screen melts that are being applied beyond the range of current $OPAM_{SAT}$
285 experiments.

286 Our $OPAM_{SAT}$ experimental dataset is combined with $OPAM_{UNSAT}$ melts from the
287 large experimental compilation of Weber and Blundy (2023). The $OPAM_{UNSAT}$ melts are those
288 experiments that contain up to two of the three major OPAM mineral phases (olivine ±
289 plagioclase ± augitic clinopyroxene) plus or minus Fe-oxides, and are performed under
290 pressurised conditions at ≤10 kbar. Further, we filter these $OPAM_{UNSAT}$ melts to ensure they

too are within the 28 OPAM convex hulls as described above. The result is an $OPAM_{UNSAT}$ dataset that is coincidentally identical in size to our $OPAM_{SAT}$ dataset (n=249), together forming our "saturation dataset" (n = 498; Fig. 2; Supplementary Table 2a; full references in Supplementary Table 2b). These 498 experiments are used to define the probability that a melt of unknown saturation state (e.g., a natural melt composition) is $OPAM_{SAT}$ given that it first satisfies the OPAM convex hull test.

The experimental data of the saturation dataset are combined with the natural (unknown) dataset to produce a single, coherent "input dataset" for comparison. Next, all melts within the input dataset have their oxide melt chemistry transformed. Raw compositional data carry only relative information and are subject to nonnegative and constant-sum (100 wt%) constraints (Boschetty et al., 2022). Instead, ratios between compositional data better measure variability which can be achieved using log-ratio transformations that map data into an unconstrained Euclidian space (Chayes, 1971). We use the isometric log ratio (ilr) which yields seven isometric log ratios (one less than the number of critical oxides) that preserve the geometric properties of the raw data and have a non-singular covariance matrix (Boschetty et al., 2022; Egozcue et al., 2003; Equation 2). The ilr is calculated using the "ilr" function in the "compositions" package (Boogaart et al., 2023) of R (R Core Team, 2023) as follows:

$$ilr(x) = \sqrt{\frac{i}{i+1}} ln\left[\frac{g(x_1, \dots, x_i)}{x_{i+1}}\right], i = 1,2, \dots . D-1 \quad (2)$$

where, x is a raw melt compositional analysis, i is a specific part, D is the total number of parts (8, the number of critical oxides), and $g(x_i)$ is the geometric mean of the parts of x given by:

$$g(x_i) = \left(\prod_{i=1}^{n} x_i\right)^{\frac{1}{n}} \quad (3)$$

Next, using the newly ilr-transformed data, a Euclidian distance matrix is calculated for the input dataset:

$$d_E = \sqrt{\sum_{i=1}^{n}(x_i - y_i)^2} \quad (4)$$

where d_E is the Euclidean distance matrix, i is the number of parts (7, the number of isometric log ratios from Equation 2), and x and y are the two compositional analyses being considered. The entire Euclidian distance matrix is normalised between 0 (closest) and 1 (furthest) according to:

$$d_{E(norm)} = \frac{d_E^i - \min(d_E)}{\max(d_E) - \min(d_E)} \quad (5)$$

where d_E^i is a single entry in the Euclidian distance matrix (d_E).

To predict whether an unknown (natural) entry in the input dataset is $OPAM_{SAT}$ or $OPAM_{UNSAT}$ we use the n closest experimental points according to the scaled distance matrix ($d_{E(norm)}$). The sensitivity to n is assessed in the results section. The n closest scaled distances are used in a weighted equation which returns the probability of OPAM saturation (P_{SAT}):

$$P_{SAT} = \sum_{i=1}^{n}\left[\left(1 - d_{E(norm)}^i\right) * {}^{V_{SAT}}/_{n}\right] \quad (6)$$

where V_{SAT} is the numerical saturation value of each of the n points (V_{SAT} = 0 for an $OPAM_{UNSAT}$ melt; V_{SAT} = 1 for an $OPAM_{SAT}$ melt). If Equation 6 returns ≥0.5 then the

unknown value is considered more likely to be $OPAM_{SAT}$ and if it returns <0.5 then it is considered more likely to be $OPAM_{UNSAT}$. The above mathematics reduces to a quantitative question, which is posed for each compositional datapoint of unknown saturation state in the input dataset in turn: "of the n closest experimental points of known saturation state to our datapoint of unknown saturation state, how many of those n experiments are $OPAM_{UNSAT}$ and how many are $OPAM_{SAT}$ in scaled multidimensional chemical space"? Equations 2 and 3 transform the experimental and unknown data, Equations 4 and 5 define distance using the newly transformed data, and Equation 6 weights the n experiments by their distances to the unknown melt. This approach has two advantages: (i) unevenly distributed experiments in *P-T-X* space are accounted for by Equation 6, giving a smaller weight to chemically distal experiments; (ii) Equation 6 has a probabilistic meaning such that an unknown melt sitting in a part of multidimensional chemical space which is occupied by many $OPAM_{SAT}$ melts will return a high saturation probability, whereas a diffuse mixture of $OPAM_{SAT}$ and $OPAM_{UNSAT}$ experiments will return a lower saturation probability.

Initial variable selection, regression methodology, and model validation

To derive an improved OPAM thermobarometer we regress new *T* and *P* equations using our $OPAM_{SAT}$ experimental compilation (n = 249; Supplementary Table 1a). Regression identifies the "best fit" equation that describes a dataset by minimising a cost function, in this case (and most typically) the sum of the squared residuals. We follow the reverse approach to multilinear regression which initially includes all possible variables in the fitting process, fits a function, identifies the variable of lowest significance, and removes it from the fit. This process is performed iteratively using the "lm" function in the "stats" package of R (R Core Team, 2023) until all variables and coefficients in the fit are significant. The t-value and p-value are the common measures of significance, where the p-value is the probability that any

observed relationship is due to chance and the t-value is the ratio between a fit coefficient and its standard error. Fit coefficients with higher t-values (e.g., >3) and low p-values (<0.01) indicate a good fit to the data. We use a stopping rule such that all variables must have t-values >3 to be considered a converged fit. A small number of additional outliers ($P = 6$; $T = 3$) were identified during the fitting process, based on residuals 1.5 times higher than the interquartile range of all residuals, and these were omitted from the regression (e.g., Blundy, 2022).

The starting variables to initialise the iterative regression process should logically describe the OPAM cotectic position as a function of *P*-*T*-*X*. The OPAM cotectic is *P*-sensitive, largely due to expansion of the clinopyroxene stability field at higher *P* (Bender et al., 1978; Grove et al., 1992; Lissenberg et al., 2019), with increasing melt H_2O content also suppressing plagioclase saturation to lower *T* at fixed *P* (Sisson and Grove, 1993; Yoder, 1965). CaO-MgO-Al_2O_3-SiO_2 (CMAS; Libourel et al., 1989; Presnall et al., 1978; Shi, 1992; Yang et al., 1996) in addition to FeO (Shi, 1993), Na_2O, K_2O, and TiO_2 (Yang et al., 1996) are the major elements which have previously been used to characterise the OPAM cotectic (i.e., the eight critical oxides used for our OPAM saturation test). Increasing Cr_2O_3 promotes clinopyroxene saturation, which prompted the reformulation of the three Yang et al (1996) cotectic equations by Voigt et al (2017). However, we omit Cr_2O_3 from our fit routine due to a lack of consistent reporting in both experimental and natural data which would prevent its wide application and robust testing. Oxides are normalised to 100 wt% (anhydrous) and converted to liquid cation fractions (e.g., $X_{AlO_{1.5}}$) for fitting (see Table 1 of Putirka, 2008 for an example conversion). Composite variables implicated by other studies of basaltic melt equilibria such as $X_{SiO_2} * X_{TiO_2}$, $\left(X_{SiO_2}\right)^2$ (Yang et al., 1996), Ca# $\left(X_{CaO}/\left[X_{CaO} + X_{NaO_{0.5}}\right]\right)$, Al# $\left(X_{AlO_{1.5}}/\left[X_{AlO_{1.5}} + X_{SiO_2}\right]\right)$ (Neave and Namur, 2022), and $X_{CaO}/X_{AlO_{1.5}}$ (Voigt et al., 2017) were also included. The latter positively correlates with clinopyroxene saturation *T* as well as the Mg# of the liquidus

clinopyroxene (Voigt et al., 2017), whereas alkalis modulate olivine stability (Grove et al., 1992; Meen, 1990).

Around 10 points or more are required per fit variable (Harrell, 2015) meaning our 13 initial variables require around 130 experiments. Therefore, we are required to split our experimental dataset into two roughly equal parts: a "training dataset" (n = 126) to regress the model and a "validation dataset" (n = 123) to recover independent performance statistics. We partition entire experimental studies into each dataset, rather than splitting all data randomly, to assess the role of systematic error between experimental studies (see Discussion). We achieve this using a splitting algorithm which repeatedly partitions studies randomly into the training and validation dataset until the number of entries in each dataset are 125±5. There is sufficient chemical overlap between the two datasets (Supplementary Fig. 1). Once the thermometer and barometer are regressed using the training dataset, the validation dataset is used to recover the following metrics of average model performance: the standard error estimate of the fit (SEE; Equation 7); the slope, intercept, and R^2 of a plot of predicted (X) versus experimental P or T (Y; Piñeiro et al., 2008); and the mean absolute error (MAE; Equation 8).

$$SEE = \sqrt{\frac{1}{N}\sum_{i=1}^{N}(predicted_i - experimental_i)^2} \qquad (Equation\ 7)$$

$$MAE = \frac{1}{N}\sum_{i=1}^{N}|predicted_i - experimental_i| \qquad (Equation\ 8)$$

Our thermobarometer and saturation test are presented as a straightforward R script which reads from an input csv file to be populated with melt data. The R script, input csv file template, and simple instructions for use (i.e., downloading R, opening and running the script)

are provided in the Supplementary Material and on the code repository GitHib (https://github.com/OJHiggins/HS2024_OPAM). The R script output retains the original data structure of the input csv file and manages unlimited additional descriptor columns (field location, sample names, etc).

RESULTS

Independent test of the Yang et al (1996) OPAM thermobarometer

To independently test the performance of the Yang et al (1996) thermobarometer we use our $OPAM_{SAT}$ compilation minus the experimental studies named in Table 4 of Yang et al (1996; n=199). The barometer calculations were made using the Yang et al (1996) implementation of Baxter et al (2023) which applies the method of Hartley et al (2018) and so also returns their probability of $OPAM_{SAT}$ (P_F). The Yang et al (1996) thermometer is not applied in Baxter et al (2023) so we instead use the liquid cation output from Baxter et al (2023) and calculate *T* ourselves using the Yang et al (1996) thermometer equation. The limit of H_2O for the Yang et al (1996) thermobarometer is not officially stated but is probably capped at ~2 wt% H_2O based on the upper concentration in their calibration experiments. To inspect the uncertainty of the Yang et al (1996) thermobarometer as a function of melt H_2O, we calculate the SEE (Equation 7) and MAE (Equation 8) for experiments with an $H_2O \leq H_2O_{max.}$ We vary H_2O_{max} between 0 and 7.2 wt% H_2O to yield an uncertainty metric of the Yang et al (1996) equations at every melt H_2O content in the test dataset. Whilst melt H_2O exceeding ~2 wt% would likely result in a significant drop in the Yang et al., (1996) thermobarometer performance given the significant melt-compositional control of melt H_2O (Fig. 1), we would expect their thermobarometer to reproduce experimental values close to the quoted uncertainties at anhydrous and low-H_2O conditions.

Of the 199 input $OPAM_{SAT}$ experiments in our Yang et al., (1996) test dataset, only 7 pass the Hartley et al (2018) saturation filter of $P_F \geq 0.8$ which is 4% of all experiments or 13% of anhydrous (0 wt% H_2O) experiments. As outlined above, our $OPAM_{SAT}$ compilation contains no obvious experimental outliers and so should be a robust test of the number of false negatives produced by an OPAM saturation classifier. Our observation is consistent with that of Baxter et al (2023) where only 92 of their 250 OPAM experiments have a $P_F \geq 0.8$ (37%) and only 23 of these were conducted at >1 atm (9%). Hartley et al (2018) deliberately tuned their P_F to limit false positives which, in a binary classifier, will be counterbalanced by a higher number of false negatives; whilst we acknowledge the important step forward by Hartley et al (2018) in the pre-screening of $OPAM_{SAT}$ melts before applying the Yang et al., (1996) thermobarometer, the false negative rate is very high and likely underrepresented by Baxter et al (2023).

The Yang et al., (1996) predicted *T* and experimental *T* show poor correspondence, with an increasing overestimation of *T* with increasing melt H_2O (Fig. 3a). The few $OPAM_{SAT}$ experiments with $P_F \geq 0.8$ (large symbols in Fig. 3a) generally lie close to the 1:1 line. Despite a strong relationship between the quality of Yang et al., (1996) *T* prediction and melt H_2O, several anhydrous experiments still show considerable and systematic *T* overestimation. The relationship between uncertainty and melt H_2O can be more clearly observed in Fig. 3b, where both the SEE and MAE increase quasi-linearly between 0 wt% H_2O (n = 53) and ≤7.2 wt% H_2O (n = 199). At anhydrous conditions, the SEE is ±35 ˚C and the MAE is ±29 ˚C which is more than the ±20 ˚C quoted by Yang et al., (1996) but comparable to many widely applied melt-based and mineral-based thermometers (e.g., Putirka, 2008). However, the Yang et al., (1996) calibration is theoretically applicable to melts with up to ~2wt% H_2O based on the calibration dataset and is often applied in low-H_2O, but not anhydrous, natural systems (e.g., Iceland, the Galápagos; Hartley et al., 2018; Stock et al., 2018). As an example, the H_2O of

matrix melts and nominally anhydrous minerals in basalts from the Galápagos span 0.06-0.77 wt% and 0.09-2.54 wt% respectively (Gleeson et al., 2021; Fig. 3b). At the upper limit of these natural melt H_2O contents, the SEE is ±69 ˚C and the MAE is ±55 ˚C in addition to the systematic uncertainty highlighted in Figure 3a.

The Yang et al., (1996) predicted *P* and experimental *P* show the same relationship as for *T* (Fig. 3c), with a systematic overestimation of predicted *P* with increasing melt H_2O. Again, the few experiments with $P_F \geq 0.8$ (large symbols in Fig. 3c) generally lie close to the 1:1 line. Contrary to the suggestion of Baxter et al (2023), we observe no strong relationship between P_F, offset between predicted and experimental P, and melt alkali content (Na_2O+K_2O [wt%]; square symbols in Fig. 3c). We question the utility of their melt alkali filter given that changing the maximum permissible Na_2O+K_2O of an input melt from 6.16 wt% to 5 wt% resulted in a reduction of only ±0.03 kbar in the MAE according to Table 1 of Baxter et al (2023). The Yang et al., (1996) MAE of ±1.13 kbar quoted by Baxter et al (2023) is a substantial underestimate; for anhydrous melts using our independent dataset the SEE is ±3.29 kbar and the MAE is ±2.54 kbar, more than double their quoted value. These results underscore the significant effect that filtering large quantities of $OPAM_{SAT}$ experiments can have on the quoted uncertainty. For H_2O contents in the range of melts from the Galápagos, the SEE and MAE rise to ±4.96 and ±3.83 kbar respectively (Gleeson et al., 2021; Fig. 3d). In short, the Yang et al (1996) barometer suffers from significant systematic (Fig. 3c) and random (Fig. 3d) uncertainty when tested by an independent $OPAM_{SAT}$ dataset, even at anhydrous conditions.

$OPAM_{SAT}$ prediction

To assess the performance of our binary classifier for $OPAM_{SAT}$ melts as a function of n, we treat each experiment from the saturation dataset (n = 498) in turn as an unknown and predict the saturation state ($OPAM_{UNSAT}$ or $OPAM_{SAT}$). We score our approach using the

number of true positives (TP), false positives (FP), true negatives (TN), and false negatives (FN). The combination of these metrics defines the accuracy (A) and precision (P) of the algorithm, as well as the true positive rate (TPR), false positive rate (FPR), true negative rate (TNR), and false negative rate (FNR) (Equation 9a–f; Fig. 4):

$$TPR = \frac{TP}{TP + FN} \qquad (Equation\ 9a)$$

$$FPR = \frac{FP}{FP + TN} \qquad (Equation\ 9b)$$

$$TNR = 1 - FPR \qquad (Equation\ 9c)$$

$$FNR = 1 - TPR \qquad (Equation\ 9d)$$

$$A = \frac{TP + TN}{TP + TN + FP + FN} \qquad (Equation\ 9e)$$

$$P = \frac{TP}{TP + FP} \qquad (Equation\ 9f)$$

The predictive performance of our OPAM binary classifier varies as a function of n, where n is the number of points considered to define the local state of OPAM saturation in multidimensional space, and can be divided into three broad behaviours (grey shading in Fig. 4; i-iii):

(i) Predictive performance is good (accuracy=0.81-0.74; precision=0.91-0.78) but erratic or "spiky" ($2 \leq n < 10$). The FPR increases with n but remains broadly low (0.06-0.20).

(ii) Classifier performance begins to drop off as n increases, with accuracy (0.75-0.63) and precision (0.81–0.70) decreasing over a wide range of n ($11 \leq n < 40$). The FNR increases and the TPR decreases in tandem but the FPR and TNR both remain stable.

(iii) All performance metrics largely plateau at $n \geq 40$, except for an increasing FNR (0.5-0.68) and decreasing TPR (0.47-0.32).

Using the calculated performance metrics, our preferred n value is 11, coinciding with the end of the spiky behaviour whilst maximising predictive performance (ii; Fig. 4; Supplementary Table 3). At n=11, our approach has an accuracy of 0.75, a precision of 0.78, a TPR of 0.7, and a FPR of 0.2. Therefore, when assessing the saturation state of a natural melt of unknown saturation state, the saturation states of the 11 closest experimental melts are considered. Our approach is not a "model" *sensu stricto*, but rather a probability map of local compositional space detailing the likelihood that a given melt is $OPAM_{SAT}$. Theoretically, our method can continuously evolve as experiments are added, particularly at the margins of the OPAM convex hulls. However, whilst the performance metrics of our model offer improvements over the original saturation test of Hartley et al (2018), our model does not unequivocally identify $OPAM_{SAT}$ melts (Fig. 4). It is highly likely that the diffuse overlap in chemical space between $OPAM_{SAT}$ and $OPAM_{UNSAT}$ melt compositions (e.g., Fig. 2) makes a perfect mathematical solution impossible. As such, our saturation test should be used in combination with petrographic and geochemical indicators where possible and should always be usurped by these methods. The key advantage of our approach is that it acknowledges the local diffuseness of the multidimensional space occupied by $OPAM_{SAT}$ and $OPAM_{UNSAT}$ melts when calculating P_{SAT}.

New OPAM thermobarometer performance

The successful fits for *P* (Equation 10a) and *T* (Equation 10b) of $OPAM_{SAT}$ melts as a function of the melt composition are as follows:

$$P(kbar) = 90.74 - (257.77 * X_{SiO_2}) + (33.99.X_{AlO_{1.5}}) + (106.83 * X_{MgO}) - (194.34.X_{CaO}) - (50.55.X_{NaO_{0.5}}) + \left(189.62.\left(X_{SiO_2}\right)^2\right) \quad (Equation\ 10a)$$

$$T(^{\circ}C) = -9201 + \left(10331 * X_{SiO_2}\right) + (7128 * X_{FeO}) + \left(10004 * X_{MgO}\right) + \left(7691 * X_{NaO_{0.5}}\right) + \left(9658 * X_{KO_{0.5}}\right) + (9574 * Al\#) + (19921 * [X_{SiO_2} * X_{TiO_2}]) + (1303 * [X_{CaO}/X_{AlO_{1.5}}]) \quad (Equation\ 10b)$$

where *X* followed by the oxide subscript denotes liquid cation fractions calculated using the method outlined in Table 1 of Putirka (2008) on an anhydrous basis, all Fe is considered as FeO, and Al# $\left(X_{AlO_{1.5}}/\left[X_{AlO_{1.5}} + X_{SiO_2}\right]\right)$ is on a molar basis. Coefficient standard errors, p-values, and t-values are listed in Supplementary Table 4, with scatter assumed to include normally distributed error (e.g., analytical and experimental uncertainty).

Performance metrics for our new OPAM thermometer and barometer are calculated using the same validation dataset (n = 123). The new thermometer has a SEE of ±35 ˚C and an MAE of ±30 ˚C, with low systematic offset relative to the 1:1 line (grey line in Fig. 5a) shown by slope (1.00) and intercept (7 ˚C) values close to 1 and 0, respectively (Fig. 5a). For the closest comparison to the quoted uncertainty of ±20 ˚C for the Yang et al (1996) thermometer, the MAE of our own training dataset is ±21 ˚C although our MAE is applicable for a much wider range of melt H_2O. The new barometer has a SEE of ±1.13 kbar and an MAE of ±0.9 kbar (Fig. 5b). As with our thermometer, the systematic offset relative to the 1:1 line of our new barometer is modest (slope = 0.98, intercept = 0.17 kbar). It is difficult to compare uncertainty with the Yang et al (1996) barometer as we have asserted that truly independent test statistics were not produced by Hartley et al (2018) or Baxter et al (2023; Fig. 3). However, the quoted uncertainty of Baxter et al (2023) on their partially self-validated and heavily filtered test dataset is an MAE of ±1.13 kbar. Our performance statistics are calculated using an independent validation dataset and are applicable to a range of melt H_2O contents spanning 0 to 7.7 wt%. Furthermore, the MAE of our new *P* calibration is similar to the quoted MAE value of the gabbronorite (CHOMPI) melt-based barometer of Blundy (2022; MAE=±1.3 kbar) and

555 the SEE of the clinopyroxene-liquid barometer of Neave and Putirka (2017; SEE=±1.4 kbar).
556 Therefore, our calibration can complement other independent models and, indeed, produces
557 comparable results (see Discussion).

558 Given the strong control of melt H_2O on the uncertainty of the Yang et al., (1996)
559 thermobarometer performance (Fig. 3), we also assess any systematic uncertainty in *P* and *T*
560 residuals (experimental *P* or *T* minus predicted *P* or *T*) for our new OPAM thermobarometric
561 equations (Equation 10a, Equation 10b) as a function of melt H_2O. As the melt H_2O
562 concentration is universally higher in volcanic arcs (Wallace, 2005) compared to mid-ocean
563 ridge basalts (MORB) and ocean island basalts (OIB; Michael, 1995; Sobolev and Chaussidon,
564 1996), we also categorise experimental studies as either arc or MORB/OIB where these labels
565 are unambiguous (Fig. 5c, Fig. 5d). When using these categories there is a tendency for the *T*
566 of OIB and MORB experiments to be underestimated, with an average residual of +24 ˚C
567 compared to a mean of +7 ˚C for arc experiments (Fig. 5c). For *P*, there is no clear relationship
568 between the calculated residuals and geodynamic setting, with relatively sharp distributions
569 centred on zero (Fig. 5d). Overall, compared to the very large effect observed for the Yang et
570 al., (1996) equations (Fig. 3), melt H_2O only weakly dictates systematic uncertainty in *T* (Fig.
571 5c) and has little effect on systematic uncertainty in *P* (Fig. 5d) for our new OPAM
572 thermobarometer.

573

574 **DISCUSSION**

575

576 **Perspectives on thermobarometer performance and usability**

577 The calibration and testing of our improved OPAM barometer (Equation 10a) and
578 thermometer (Equation 10b) as a function of $OPAM_{SAT}$ melt composition has highlighted three
579 considerations for future thermobarometers.

In a correlation matrix between SiO_2, TiO_2, Al_2O_3, FeO, MgO, CaO, Na_2O, K_2O, *T*, and *P* using our newly compiled $OPAM_{SAT}$ dataset (n=249; Supplementary Fig. 2), P is the third most correlated variable with *T* and *T* is the most correlated variable with *P* (correlation coefficient = 0.51). The original Yang et al., (1996) thermometer regresses *T* as a function of $OPAM_{SAT}$ melt composition and *P*, in contrast to Equation 10b which is a *P*-independent thermometer. Whilst the addition of a *P* term undoubtedly leads to an improved fit for many thermometers (e.g., Neave and Putirka, 2017; Putirka, 2016, 2008), the incorporation of a *P* term makes it difficult to deconvolve whether any relationship between *P* and *T* is methodological or thermodynamic. In other words, can *P* and *T* be considered two truly independent variables? The strong correlation between *P* and *T* is a thermodynamic consequence for high-melt-fraction, hydrous experiments close to the liquidus due to the strong dependency of volatile solubility and *P* on liquidus *T* (Bohlen et al., 1982). However, in lower-melt-fraction experiments further from the liquidus, some of the correlation between *P* and *T* will also be partly due to the methodological tendency to perform high-*T* experiments at lower *P* and vice versa. This tendency relates to the need for experimentalists to have large melt pools to analyse in their experimental charges, requiring a methodological consideration of liquidus *T* which is a function of *P*. By applying *P*-dependent thermometers and *T*-dependent barometers in natural systems, this experimental bias may consequently be introduced into geological interpretations of natural systems, leading to spurious correlations between the two variables. Therefore, we advise that *P* and *T* remain purely independent when calibrating thermobarometers, or that both dependent and independent equations are provided where alternative constraints on *P* or *T* are available (e.g., Putirka, 2016).

Our binary classifier to determine the probability that a melt is $OPAM_{SAT}$ highlights the need for new standards in how binary classifiers are benchmarked and tested between studies. In the case of testing thermobarometric equations (e.g., Equation 10a, Equation 10b),

605 the SEE (Equation 2) and MAE (Equation 3) are standardised metrics which can robustly
606 compare different thermobarometer performance between studies (e.g., Fig. 3, Fig. 5). In
607 contrast, testing classifiers requires a clear description of prior assumptions, akin to the prior
608 assumption term described in the equation of Bayes Theorem. For example, the performance
609 metrics for our new binary classifier outlined in Figure 4, such as the accuracy and precision,
610 are valid for the prior assumptions that: (i) the experimental melt is in equilibrium with between
611 one and three of olivine + plagioclase + clinopyroxene, with or without Fe-oxides; (ii) the melt
612 of unknown saturation state, be it a newly performed experimental melt or a natural melt
613 composition, passes the OPAM convex hull test. The latter assumption is determined
614 mathematically by our model and marked in the output csv files generated by our R script, yet
615 the former requires at least some petrographic or geochemical knowledge from the user prior
616 to model application. Consistently stating these prior assumptions is vital if the performance
617 of future new and improved OPAM classifiers are to be fairly and consistently compared with
618 existing models.

619 The residuals for experimental P or T minus predicted P or T of our new models are
620 generally centred at or close to zero and there is little systematic uncertainty identified by the
621 fit between predicted and measured values (Fig. 5). Despite this, there is clear clustering of
622 individual studies on either side of the 1:1 line between predicted and experimental P or T (Fig.
623 5), demonstrating that inter-study effects partly control the thermobarometer uncertainty
624 according to the validation dataset statistics. This intra-study clustering effect is often apparent
625 in machine learning thermobarometers where multiple train-validation dataset splits show the
626 effect that partitioning of studies between these two datasets can have on model performance
627 (Higgins et al., 2021a; Jorgenson et al., 2022; Petrelli et al., 2020). Understanding,
628 constraining, and correcting for these inter-study or inter-laboratory effects is central to

developing future barometers which can reliably predict global datasets with uncertainties comparable to those quoted for the original regression.

Application to two geophysically monitored volcanic eruptions

The *P-T-X* of magma during storage and ascent plays a leading role in modulating eruptive dynamics (Higgins and Caricchi, 2023; Popa et al., 2021). Therefore, quantitative tools to describe pre-eruptive magmatic *P-T-X*, such as the new thermobarometric equations presented here, can be useful to: (i) petrologically monitor active volcanoes during protracted eruptions, particularly to compare evolving geochemical and geophysical signals (Hartley et al., 2018; Longpré et al., 2014; Magee et al., 2018, 2020; Saunders et al., 2012; Stock et al., 2018); (ii) understand medium-term and long-term evolution in magma storage conditions by studying multiple temporally constrained volcanic deposits (Bouvet de Maisonneuve et al., 2021; Forni et al., 2018; Giordano and Caricchi, 2022; Higgins et al., 2021a; Smithies et al., 2023; Weber et al., 2020). To assess the utility of our new thermobarometer for studying volcanic systems, we apply our calibration to the $OPAM_{SAT}$ melts of two case study eruptions (the 2015 eruption of Wolf Volcano, Galápagos; the 2014-2015 Holuhraun eruption, Iceland). Both eruptions have been geophysically, geochemically, and petrographically studied in detail, providing a means of independent validation and comparison with our updated thermobarometric predictions. For the two case study eruptions we present *P* and *T* predictions with our new thermobarometer for both unfiltered (all samples which pass the OPAM convex hull test; n = 76 of 76 for Wolf and n = 102 of 114 for Holuhraun) and filtered ($P_{SAT} \geq 0.5$; n = 70 of 76 for Wolf and n = 45 of 102 for Holuhraun) data. In doing so we keep track of any compositional bias, if present, introduced to our *P* and *T* predictions by the probabilistic filtering. The full dataset of melt compositions for both volcanic systems are presented in Supplementary Table 5.

654

655 *The 2015 eruption of Wolf Volcano, Galápagos*

656 The Galápagos Archipelago is one of the most volcanically active regions on Earth,
657 with eruptions occurring at a repose period of ~2 years (Bernard et al., 2019). The archipelago
658 is the surface manifestation of the Galápagos plume which impinges on the base of ~10 Ma-
659 old, ~11 km-thick oceanic crust (Feighner and Richards, 1994). Wolf Volcano, on the north of
660 Isabela Island, is an active volcano in the western Galápagos (Geist et al., 2005). The 2015
661 eruption produced ~0.01 km^3 of monotonous basaltic lava and tephra from circumferential and
662 radial vents (Bernard et al., 2019; Stock et al., 2020, 2018). We apply our new OPAM
663 thermobarometer to the 2015 whole rock and matrix glass measurements from Wolf Volcano
664 (Stock et al., 2020, 2018). All petrological *P* (kbar) estimates are converted to depth (km)
665 relative to the surface using a polynomial fit to the Hawaiian ocean crust *P*-depth relationship
666 of Putirka (1997; Equation 11; $R^2 = 0.96$) as per Stock et al. (2018):

667

668 $$Depth\ (km) = -0.02086^2.P(kbar) + 3.36352.P(kbar) + 0.46170 \quad (Equation\ 11)$$

669

670 All whole rock and matrix glass data bar six measurements return a strong indicator for OPAM
671 saturation (P_{SAT}) using our new saturation test (0.81±0.16; mean±1σ), agreeing with
672 petrographic and thermodynamic modelling results which attest to three-phase saturation
673 (Stock et al., 2020). Due to the strong indication for OPAM saturation in all samples, unfiltered
674 and filtered ($P_{SAT} \geq 0.5$) melts record an identical *T* of 1151±15 ˚C (mean±1σ) using Equation
675 10b (Fig. 6a). The restricted whole rock compositions result in a tighter range of *T* (1172±2
676 ˚C) compared to matrix glass (1144±11 ˚C). The overall $OPAM_{SAT}$ T range is in strong
677 agreement with clinopyroxene thermometry for glomerocrystic (1164±11 ˚C), phenocrystic
678 (1151±9 ˚C), and tephra-hosted (1164±15 ˚C) clinopyroxene from Stock et al. (2018; Fig. 6a).

New OPAM P estimates for unfiltered Wolf samples (n = 76), calculated with Equation 10a and converted to depth (km) using Equation 11, are 8.6±2.2 km for matrix glass and 9.6±0.8 km for whole rock. The $OPAM_{SAT}$ depths compare well with estimates derived using the Yang et al., (1996) barometer and $P_F \geq 0.8$ filter of Hartley et al., (2018; 9.7±2.8 km; A and B vs L in Fig. 6b). Filtering our new $OPAM_{SAT}$ depths ($P_{SAT} \geq 0.5$; n=70) yields near identical values for matrix glass (8.6±2.3 km; C in Fig. 6b) and identical values for whole rock (9.6±0.8 km; D in Fig. 6b) compared to the unfiltered results. The three different textural sub-classes of clinopyroxene identified by Stock et al. (2018) record appreciably wider and systematically deeper storage depths (glomerocrystic = 9.7±2.5 km, phenocrystic = 11±2.8 km, tephra-hosted = 10±3.1 km; mean±1σ; I, J, and K in Fig. 6b), where P is calculated using clinopyroxene-melt barometry (Neave and Putirka, 2017). Inversion of interferometric synthetic aperture radar (InSAR) measurements indicates a shallow source at ~1 km depth (E in Fig. 6b) and deep sources at ~6.1 to 8.8 km (F, G, and H in Fig. 6b). Encouragingly, our new OPAM barometer produces depth results which are consistent with the depth of the deep magma source identified by InSAR inversion (F, G and H in Fig. 6a). Therefore, we corroborate the findings of Stock et al (2018) that magmas feeding the 2015 Wolf eruption were sourced predominantly from the lower crust and not the shallow-crustal InSAR source at ~1 km (E in Fig. 6b). In detail, the mean values of all petrographic indicators of magma storage depth (pressure) are systematically higher than those from the InSAR inversions. As alluded to by Stock et al (2018), we interpret this offset as InSAR signals returning deformation specifically at the top of a vertically protracted magma storage region whereas petrological estimates are recording crystallisation and/or equilibration deeper within that same storage region. We note that the mean depths recovered using our new OPAM barometer are most consistent with the InSAR results (Fig. 6b).

The 2014-2015 Holuhraun eruption, Iceland

The island of Iceland is the surface expression of a plume-ridge interaction between the Mid-Atlantic Ridge and a mantle plume, resulting in anomalously thickened oceanic crust (15-44 km; Darbyshire et al., 2000; Jenkins et al., 2018) due to an increased mantle potential temperature that enhances melt supply. A variable mantle melt flux has been posited as a control on magma storage pressures on Iceland (Baxter et al., 2023), producing highly variable depths for the erupted melts from various volcanic zones. The 2014-2015 Holuhraun eruption was a basaltic fissure event that originated from within the Bárðarbunga volcanic system in central Iceland, producing >1.4 km^3 of lava and tephra (Pedersen et al., 2017). The eruption represents a remarkable case study for testing models of magma storage conditions due to extensive pre- and syn-eruptive geochemical, seismic, and ground deformation datasets (Ágústsdóttir et al., 2016; Gauthier et al., 2016; Gudmundsson et al., 2016; Halldórsson et al., 2018; Hartley et al., 2018; Sigmundsson et al., 2015). Further, it allows us to directly verify our new OPAM thermobarometer against the results of Hartley et al. (2018), who developed their implementation of the Yang et al., (1996) barometer to assess the evolution of magma storage depths during the 6-month Holuhraun eruption. We apply our new OPAM thermobarometer to melt inclusion and matrix glass measurements from the Holuhraun eruption and, for direct comparison with Hartley et al. (2018), our *P* (kbar) estimates are converted to depth (km) relative to the surface using a fixed crustal density of 2.86×10^6 kg/m^3.

Unlike samples from Wolf Volcano (Fig. 6a), Holuhraun melts show a lower and more diverse range of P_{SAT} using our new saturation test (0.46±0.19; mean±1σ; Fig. 7a). Considering all compositions unfiltered for P_{SAT} (n = 102), *T* ranges from 1135 to 1254 ˚C (1193±31 ˚C) except for a single outlier at 1098 ˚C (Fig. 7a). Three *P* values, not plotted but included in the *P* statistics, return negative *P* estimates. When our new OPAM *P* results are converted to depth, unfiltered matrix glass (7.1±1.7 km; A in Fig. 7b) and melt inclusions (8.8±4.4 km; B in Fig.

7b) overlap. Using a filter of $P_{SAT} \geq 0.5$ (n = 45), only 2 of 9 matrix glass values remain (5.2 km and 8.7 km; C in Fig. 7b), whereas melt inclusions cover a similar range to the unfiltered data (9.3±4.7 km; D in Fig. 7b). The wide spread of the melt inclusion depths is consistent with clinopyroxene-liquid barometry (Neave and Putirka, 2017) applied to clinopyroxene crystals that were screened for textural equilibrium (Halldórsson et al., 2018; 8.2±5 km; G in Fig. 7b).

The unfiltered depth results of the Yang et al (1996) equations implemented by Hartley et al (2018) are similar to our unfiltered OPAM depths for both matrix glass (6.6±2.4 km; H in Fig. 7b) and melt inclusions (10.2±4.2 km; I in Fig. 7b). However, the Hartley et al (2018) OPAM depths filtered for $P_f \geq 0.8$ are notably deeper and less dispersed for melt inclusions (11.9±3.5 km; K in Fig. 7b) compared to their unfiltered values, whereas matrix glass (6.8±2.4 km; J in Fig. 7b) are near identical to their unfiltered values. This observation shows that the saturation filter of Hartley et al (2018) has a much stronger effect on skewing P to higher values for certain melt compositions than our new saturation test (Fig. 7b). Given the very-high false negative rate of the saturation test of Hartley et al (2018) there may be a compositional bias which is artificially deepening values as a result of applying their probabilistic filter. As with observations from Wolf Volcano, our OPAM barometry results are consistent with independent geophysical estimates of magma storage via the range of pre-eruptive seismicity (3-9 km; Sigmundsson et al., 2015) and the most common earthquake hypocentral depth (6±1 km; Ágústsdóttir et al., 2016), particularly for matrix glass. Therefore, we concur with Hartley et al (2018) that the 2014-2015 Holuhraun eruption represents a case study in which petrological and geophysical data can be reconciled.

CONCLUSIONS

We have calibrated a new barometer (Equation 10a) and thermometer (Equation 10b) for melts equilibrated with the mineral assemblage of olivine + plagioclase + augitic

clinopyroxene ± Fe-oxides, using an expanded dataset of anhydrous and hydrous experiments (Fig. 1, Fig. 2). The necessity to calibrate an updated OPAM thermobarometer arises from the most widely used calibration (Yang et al., 1996) being unable to reliably reproduce an independent dataset of experimental pressures and temperatures (Fig. 3). Previous attempts to calculate the true predictive performance of the Yang et al (1996) barometer by Hartley et al (2018) and Baxter et al., (2023) were hindered by: (i) testing datasets which were not independent of the Yang et al (1996) calibration dataset; and (ii) a statistical filtering process for OPAM saturation which removed large swathes of experiments that were demonstrably suitable for OPAM barometry. Therefore, the mean absolute error (MAE) of ±1.13 kbar quoted by Baxter et al., (2023) for the Yang et al (1996) barometer is a substantial underestimate. Rather, our independent test dataset yielded a MAE of ±2.54 kbar and a SEE of ±3.29 for the Yang et al (1996) barometer which increases significantly with melt H_2O (Fig. 3d). The Yang et al., (1996) thermometer performs passably at anhydrous conditions (SEE = ±35 ˚C; MAE = ±29 ˚C) but the uncertainty increases dramatically with increasing melt H_2O even at concentrations well within the range of their original calibration dataset (Fig. 3b).

In contrast with the Yang et al (1996) *P* and *T* equations, our new OPAM barometer and thermometer accurately reproduce an independent validation dataset of *P* and *T*, with a SEE of ±1.1 kbar and ±35 ˚C, respectively, and low systematic offset between measured and predicted values (Fig. 5a, Fig. 5b). Importantly we also see no significant systematic *P* offset as a function of H_2O (Fig. 5d) up to 7.7 wt% in $OPAM_{SAT}$ melts (Fig. 1), and only minor *T* offset which is within the average thermometer uncertainty (Fig. 5c). We also provide a binary classifier to predict the probability that a melt of unknown saturation state is OPAM saturated based on a weighted distance matrix in multidimensional chemical space. Our new method improves on existing approaches, particularly with respect to false negatives (falsely predicting that a melt is not $OPAM_{SAT}$), yielding an accuracy of 0.75 and a precision of 0.78 (Fig. 4). The

779 new binary classifier of OPAM saturation should be used in conjunction with detailed
780 petrographic and geochemical analysis where possible, owing to the overlap of $OPAM_{SAT}$ and
781 $OPAM_{UNSAT}$ melts in multidimensional chemical space which precludes the development of a
782 perfectly efficient binary chemical classifier (Fig. 2). Our thermobarometer and saturation test
783 are presented as a simple R script (R Core Team, 2023) which takes user input via a csv file of
784 melt compositional data.

785 To test our implementation, we used two recent volcanic eruptions which have been
786 petrographically, geochemically, and geophysically well studied (the 2015 eruption of Wolf
787 Volcano, Isabela Island, Galápagos; the 2014-2015 Holuhraun eruption, Iceland). In both
788 cases, our updated OPAM barometer is consistent with existing, independent petrological and
789 geophysical magma depth estimates but provides constraints with the lowest uncertainties to
790 date (Fig. 6, Fig. 7). Hence, given the relative ease and rapidity of whole-rock and glass analysis
791 afforded by modern sample preparation and analytical equipment, our new thermobarometer
792 can complement syn-eruptive geophysical measurements to aid hazard management during on-
793 going volcanic crises (Re et al., 2021). Additionally, our calibration may have sufficient *P* and
794 *T* resolution (SEE of ±1.1 kbar and ±35 ˚C, respectively) to identify discrete changes in magma
795 storage conditions when studying the time-integrated stratigraphic record of past eruptions.
796
797 **FIGURE CAPTIONS**
798
799 Fig.1: (**a**) Temperature (˚C) versus pressure (kbar); (**b**) melt MgO (wt%) versus melt
800 CaO/Al_2O_3; and (**c**) melt SiO_2 (wt%) versus melt Na_2O+K_2O (wt%) for $OPAM_{SAT}$ equilibrium
801 experiments, colour contoured for melt H_2O (wt%). Grey symbols are hydrous experiments for
802 which a H_2O content is not reported. Diamonds are experiments from studies used to calibrate
803 the Yang et al (1996) cotectic equations. The black curvilinear boundary in (c) is the alkaline-

804 subalkaline transition boundary (Irvine and Baragar, 1971). Melt compositions are normalised
805 to 100 wt% anhydrous with all Fe as FeO.
806
807 Fig. 2: (**a**) Melt SiO_2 (wt%) versus melt Al_2O_3 (wt%); and (**b**) melt SiO_2 (wt%) versus melt
808 MgO (wt%) for $OPAM_{SAT}$ and $OPAM_{UNSAT}$. $OPAM_{SAT}$ experiments were compiled for this
809 study and are presented in Supplementary Table 1a. $OPAM_{UNSAT}$ experiments (olivine ±
810 plagioclase ± augitic clinopyroxene ±Fe-oxides) are from the compilation of Weber and
811 Blundy (2023; Supplementary Table 2a). The OPAM convex hull is a polygon connecting the
812 outermost OPAM-saturated points in X-Y space with ±5% relative added to account for
813 analytical uncertainty (black field in both figures). Melts from the 2015 eruption of Wolf
814 Volcano (Galápagos; Stock et al., 2018, 2020) and the 2014-2015 Holuhraun eruption (Iceland;
815 Hartley et al., 2018) are also plotted (see Discussion; Supplementary Table 5). All experimental
816 and natural melt compositions are plotted normalised to the 8 critical oxides used for the OPAM
817 saturation test.
818
819 Fig. 3: Performance of the Yang et al (1996) thermometer and barometer for an independent
820 test of 199 $OPAM_{SAT}$ experiments from studies not used in the original Yang et al (1996)
821 calibration. (**a**) The predicted temperature (˚C) versus experimental temperature (˚C). (**b**) The
822 SEE and MAE for temperature (˚C) as a function of melt H_2O (wt%). The line for n shows the
823 number of experiments with the corresponding melt H_2O content on the x axis or less used to
824 calculate the SEE or MAE. (**c**) The predicted pressure (kbar) versus experimental pressure
825 (kbar). (**d**) The SEE and MAE for pressure (kbar) as a function of melt H_2O (wt%). In (a) and
826 (c) points are colour coded for melt H_2O (wt%) and large symbols indicate experiments which
827 pass the statistical filter of Hartley et al (2018) with a $P_F \geq 0.8$ (see text for details). Solid line is
828 1:1 and dashed lines are the bounds of the quoted uncertainty for the Yang et al (1996)

thermometer (±20 ˚C) and barometer (±1.13 kbar) respectively. In (b) and (d) the ranges of H_2O (wt%) measured for Galápagos melts and calculated from nominally anhydrous minerals are shown (Gleeson et al., 2021).

Fig. 4: Performance (Equation 9a-9f) of our statistical test for $OPAM_{SAT}$ melts as a function of n (the number of adjacent experiments considered in multidimensional space when testing if a natural melt is $OPAM_{SAT}$). Grey boxes (i, ii, iii) highlight changes in test performance as a function of n and are discussed in text. The chosen n used for our statistical test is 11 (thick dashed line) at the start of region (ii).

Fig. 5: The performance of our new OPAM thermobarometer using the compiled training and validation data (Supplementary Table 1a). (**a**) Experimental temperature (˚C) versus predicted temperature (˚C). (**b**) Experimental pressure (kbar) versus predicted pressure (kbar). (**c**) Experimental temperature (˚C) minus predicted temperature (˚C) and (**d**) experimental pressure (kbar) minus predicted pressure (kbar) as a function of classified geodynamic setting (lines) and experimental melt H_2O (wt%; points). In (a) and (b) summary statistics for training (grey points) and validation (coloured points) datasets are provided in the plot area. Grey solid line is the 1:1 line, black dashed lines are the bounds of the quoted validation SEE, and the black solid line is a linear fit between predicted (x) and experimental (y) values. In (c) and (d) geodynamic settings for experimental studies are either arc or ocean island basalt (OIB) plus mid-ocean ridge basalt (MORB).

Fig. 6: (**a**) Pressure (kbar) versus temperature (˚C) using our new OPAM thermobarometer for all matrix glass and whole rock data from the 2015 eruption of Wolf Volcano (Galápagos; Stock et al., 2018). Data points are colour contoured for P_{SAT} using our binary classifier for

854 $OPAM_{SAT}$ melts. Clinopyroxene *T* for the three textural subclasses of clinopyroxene from
855 Stock et al., (2018) are shown as mean±1σ ranges for comparison. (**b**) *P* converted to depth
856 using Equation 11 for petrological and geophysical methods discussed in text, with letters
857 corresponding as follows: A = mean±1σ of all matrix glass values using Equation 10a; B =
858 mean±1σ of all whole rock values using Equation 10a; C = mean±1σ of matrix glass values
859 with P_{SAT}≥0.5 using Equation 10a; D = mean±1σ of whole rock values with P_{SAT}≥0.5 using
860 Equation 10a; E = pre-eruptive shallow source from Stock et al., (2018) using InSAR; F, G, H
861 = syn-eruptive deep source of the circumferential fissure phase, caldera fill phase, and the entire
862 eruption, respectively, from Stock et al., (2018) using InSAR; I, J, K = clinopyroxene-liquid
863 barometry (Neave and Putirka, 2017) for glomerocrystic, phenocrystic, and tephra-hosted
864 clinopyroxene, respectively, from Stock et al., (2018). The Moho depth is shown by the dashed
865 line (Feighner and Richards, 1994).
866
867 Fig. 7: (**a**) Pressure (kbar) versus temperature (˚C) using our new OPAM thermobarometer for
868 all matrix glass and melt inclusion data from the 2014-2015 Holuhraun eruption (Iceland;
869 Hartley et al., 2018). Data points are colour contoured for P_{SAT} using our binary classifier for
870 $OPAM_{SAT}$ melts. (**b**) *P* converted to depth using a fixed density of $2.86*10^6$ kg/m^3 for
871 petrological and geophysical methods discussed in text, with letters corresponding as follows:
872 A = mean±1σ of all matrix glass values using Equation 10a; B = mean±1σ of all melt inclusion
873 values using Equation 10a; C = mean±1σ of matrix glass values with P_{SAT}≥0.5 using Equation
874 10a; D = mean±1σ of melt inclusion values with P_{SAT}≥0.5 using Equation 10a; E = pre-eruptive
875 seismicity (Sigmundsson et al., 2015); F = most common earthquake hypocentral depth
876 (Ágústsdóttir et al., 2016); G = clinopyroxene-liquid barometry (Neave and Putirka, 2017) for
877 clinopyroxene crystals screened for textural equilibrium (Halldórsson et al., (2018); H, I =
878 OPAM barometry of glass and melt inclusions respectively using the Yang et al (1996)

879 equations implemented by the approach of Hartley et al (2018); J, K = as for H and I but with
880 data filtered for $P_f \geq 0.8$ according to the saturation test of Hartley et al (2018).
881
882 **DATA AVAILABILITY**
883 The data tables used in this article and additional supplementary figures described in text are
884 available in its online supplementary material. The OPAM thermobarometer code and
885 saturation test are available on GitHub as a combined R script
886 (https://github.com/OJHiggins/HS2024_OPAM).
887
888 **ACKNOWLEDGEMENTS**
889 Many thanks to Gregor Weber for compiling and sharing his experimental dataset for the
890 saturation test. This study has benefitted from useful discussion with Lydia Whittaker, Tom
891 Sheldrake, Alessandro Musu, Corin Jorgenson, and Luca Caricchi. Oliver Higgins would like
892 to gratefully acknowledge the Swiss National Science Foundation for funding through an Early
893 Postdoc. Mobility Fellowship (Project Number: P500PN_210239). This publication has
894 emanated from research supported in part by a research grant from Science Foundation Ireland
895 and the Geological Survey of Ireland under the SFI Frontiers for the Future Programme
896 20/FFP-P/8895 (awarded to Michael. J. Stock).
897
898 **REFERENCES**
899 Ágústsdóttir, T., Woods, J., Greenfield, T., Green, R.G., White, R.S., Winder, T., Brandsdóttir,
900 B., Steinthórsson, S., Soosalu, H., 2016. Strike-slip faulting during the 2014
901 Bárðarbunga-Holuhraun dike intrusion, central Iceland. Geophysical Research Letters
902 43, 1495–1503. https://doi.org/10.1002/2015GL067423
903 Almeev, R.R., Holtz, F., Koepke, J., Parat, F., 2012. Experimental calibration of the effect of
904 H2O on plagioclase crystallization in basaltic melt at 200 MPa. American Mineralogist
905 97, 1234–1240. https://doi.org/10.2138/am.2012.4100

Almeev, R.R., Holtz, F., Koepke, J., Parat, F., Botcharnikov, R.E., 2007. The effect of H2O on olivine crystallization in MORB: Experimental calibration at 200 MPa. American Mineralogist 92, 670–674. https://doi.org/10.2138/am.2007.2484

Baker, D.R., Eggler, D.H., 1987. Compositions of anhydrous and hydrous melts coexisting with plagioclase, augite, and olivine or low-Ca pyroxene from 1 atm to 8 kbar; application to the Aleutian volcanic center of Atka. American Mineralogist 72, 12–28.

Baxter, R.J.M., Maclennan, J., Neave, D.A., Thordarson, T., 2023. Depth of Magma Storage Under Iceland Controlled by Magma Fluxes. Geochemistry, Geophysics, Geosystems 24, e2022GC010811. https://doi.org/10.1029/2022GC010811

Bell, A.F., La Femina, P.C., Ruiz, M., Amelung, F., Bagnardi, M., Bean, C.J., Bernard, B., Ebinger, C., Gleeson, M., Grannell, J., Hernandez, S., Higgins, M., Liorzou, C., Lundgren, P., Meier, N.J., Möllhoff, M., Oliva, S.-J., Ruiz, A.G., Stock, M.J., 2021. Caldera resurgence during the 2018 eruption of Sierra Negra volcano, Galápagos Islands. Nat Commun 12, 1397. https://doi.org/10.1038/s41467-021-21596-4

Bender, J.F., Hodges, F.N., Bence, A.E., 1978. Petrogenesis of basalts from the project FAMOUS area: experimental study from 0 to 15 kbars. Earth and Planetary Science Letters 41, 277–302. https://doi.org/10.1016/0012-821X(78)90184-X

Bernard, B., Stock, M.J., Coppola, D., Hidalgo, S., Bagnardi, M., Gibson, S., Hernandez, S., Ramón, P., Gleeson, M., 2019. Chronology and phenomenology of the 1982 and 2015 Wolf volcano eruptions, Galápagos Archipelago. Journal of Volcanology and Geothermal Research 374, 26–38. https://doi.org/10.1016/j.jvolgeores.2019.02.013

Blundy, J., 2022. Chemical Differentiation by Mineralogical Buffering in Crustal Hot Zones. Journal of Petrology 63, egac054. https://doi.org/10.1093/petrology/egac054

Blundy, J., Cashman, K., 2008. Petrologic Reconstruction of Magmatic System Variables and Processes. Reviews in Mineralogy and Geochemistry 69, 179–239. https://doi.org/10.2138/rmg.2008.69.6

Bohlen, S.R., Boettcher, A.L., Wall, V.J., 1982. The system albite–H2O–CO2: a model for melting and activities of water at high pressures. American Mineralogist 67, 451–462.

Boogaart, K.G. van den, Tolosana-Delgado, R., Bren, M., 2023. compositions: Compositional Data Analysis.

Boschetty, F.O., Ferguson, D.J., Cortés, J.A., Morgado, E., Ebmeier, S.K., Morgan, D.J., Romero, J.E., Silva Parejas, C., 2022. Insights Into Magma Storage Beneath a Frequently Erupting Arc Volcano (Villarrica, Chile) From Unsupervised Machine Learning Analysis of Mineral Compositions. Geochemistry, Geophysics, Geosystems 23, e2022GC010333. https://doi.org/10.1029/2022GC010333

Bouvet de Maisonneuve, C., Forni, F., Bachmann, O., 2021. Magma reservoir evolution during the build up to and recovery from caldera-forming eruptions – A generalizable model? Earth-Science Reviews 218, 103684. https://doi.org/10.1016/j.earscirev.2021.103684

Cashman, K., Blundy, J., 2013. Petrological cannibalism: the chemical and textural consequences of incremental magma body growth. Contrib Mineral Petrol 166, 703–729. https://doi.org/10.1007/s00410-013-0895-0

Chayes, F., 1971. Ratio Correlation: A Manual for Students of Petrology and Geochemistry. University of Chicago Press.

Darbyshire, F.A., White, R.S., Priestley, K.F., 2000. Structure of the crust and uppermost mantle of Iceland from a combined seismic and gravity study. Earth and Planetary Science Letters 181, 409–428. https://doi.org/10.1016/S0012-821X(00)00206-5

Dungan, M.A., Rhodes, J.M., 1978. Residual glasses and melt inclusions in basalts from DSDP Legs 45 and 46: Evidence for magma mixing. Contr. Mineral. and Petrol. 67, 417–431. https://doi.org/10.1007/BF00383301

Egozcue, J.J., Pawlowsky-Glahn, V., Mateu-Figueras, G., Barceló-Vidal, C., 2003. Isometric Logratio Transformations for Compositional Data Analysis. Mathematical Geology 35, 279–300. https://doi.org/10.1023/A:1023818214614

Feighner, M.A., Richards, M.A., 1994. Lithospheric structure and compensation mechanisms of the Galápagos Archipelago. Journal of Geophysical Research: Solid Earth 99, 6711–6729. https://doi.org/10.1029/93JB03360

Forni, F., Degruyter, W., Bachmann, O., De Astis, G., Mollo, S., 2018. Long-term magmatic evolution reveals the beginning of a new caldera cycle at Campi Flegrei. Science Advances 4, eaat9401. https://doi.org/10.1126/sciadv.aat9401

Gauthier, P.-J., Sigmarsson, O., Gouhier, M., Haddadi, B., Moune, S., 2016. Elevated gas flux and trace metal degassing from the 2014–2015 fissure eruption at the Bárðarbunga volcanic system, Iceland. Journal of Geophysical Research: Solid Earth 121, 1610–1630. https://doi.org/10.1002/2015JB012111

Geist, D.J., Naumann, T.R., Standish, J.J., Kurz, M.D., Harpp, K.S., White, W.M., Fornari, D.J., 2005. Wolf Volcano, Galápagos Archipelago: Melting and magmatic evolution at the margins of a mantle plume. Journal of Petrology 46, 2197–2224.

Giordano, G., Caricchi, L., 2022. Determining the State of Activity of Transcrustal Magmatic Systems and Their Volcanoes. Annual Review of Earth and Planetary Sciences 50, null. https://doi.org/10.1146/annurev-earth-032320-084733

Gleeson, M.L.M., Gibson, S.A., Stock, M.J., 2021. Constraints on the behaviour and content of volatiles in Galápagos magmas from melt inclusions and nominally anhydrous minerals. Geochimica et Cosmochimica Acta. https://doi.org/10.1016/j.gca.2021.11.005

Grove, T.L., Kinzler, R.J., Bryan, W.B., 1992. Fractionation of mid-ocean ridge basalt (MORB). Washington DC American Geophysical Union Geophysical Monograph Series 71, 281–310. https://doi.org/10.1029/GM071p0281

Gudmundsson, M.T., Jónsdóttir, K., Hooper, A., Holohan, E.P., Halldórsson, S.A., Ófeigsson, B.G., Cesca, S., Vogfjörd, K.S., Sigmundsson, F., Högnadóttir, T., Einarsson, P., Sigmarsson, O., Jarosch, A.H., Jónasson, K., Magnússon, E., Hreinsdóttir, S., Bagnardi, M., Parks, M.M., Hjörleifsdóttir, V., Pálsson, F., Walter, T.R., Schöpfer, M.P.J., Heimann, S., Reynolds, H.I., Dumont, S., Bali, E., Gudfinnsson, G.H., Dahm, T., Roberts, M.J., Hensch, M., Belart, J.M.C., Spaans, K., Jakobsson, S., Gudmundsson, G.B., Fridriksdóttir, H.M., Drouin, V., Dürig, T., Aðalgeirsdóttir, G., Riishuus, M.S., Pedersen, G.B.M., van Boeckel, T., Oddsson, B., Pfeffer, M.A., Barsotti, S., Bergsson, B., Donovan, A., Burton, M.R., Aiuppa, A., 2016. Gradual caldera collapse at Bárdarbunga volcano, Iceland, regulated by lateral magma outflow. Science 353, aaf8988. https://doi.org/10.1126/science.aaf8988

Halldórsson, S.A., Bali, E., Hartley, M.E., Neave, D.A., Peate, D.W., Guðfinnsson, G.H., Bindeman, I., Whitehouse, M.J., Riishuus, M.S., Pedersen, G.B.M., Jakobsson, S., Askew, R., Gallagher, C.R., Guðmundsdóttir, E.R., Gudnason, J., Moreland, W.M., Óskarsson, B.V., Nikkola, P., Reynolds, H.I., Schmith, J., Thordarson, T., 2018.

Petrology and geochemistry of the 2014–2015 Holuhraun eruption, central Iceland: compositional and mineralogical characteristics, temporal variability and magma storage. Contrib Mineral Petrol 173, 64. https://doi.org/10.1007/s00410-018-1487-9
Harrell, F.E., 2015. Regression Modeling Strategies: With Applications to Linear Models, Logistic and Ordinal Regression, and Survival Analysis, Springer Series in Statistics. Springer International Publishing, Cham. https://doi.org/10.1007/978-3-319-19425-7
Hartley, M.E., Bali, E., Maclennan, J., Neave, D.A., Halldórsson, S.A., 2018. Melt inclusion constraints on petrogenesis of the 2014–2015 Holuhraun eruption, Iceland. Contrib Mineral Petrol 173, 10. https://doi.org/10.1007/s00410-017-1435-0
Helz, R.T., Thornber, C.R., 1987. Geothermometry of Kilauea Iki lava lake, Hawaii. Bull Volcanol 49, 651–668. https://doi.org/10.1007/BF01080357
Herzberg, C., 2004. Partial Crystallization of Mid-Ocean Ridge Basalts in the Crust and Mantle. Journal of Petrology 45, 2389–2405. https://doi.org/10.1093/petrology/egh040
Higgins, O., Caricchi, L., 2023. Eruptive dynamics reflect crustal structure and mantle productivity beneath volcanoes. Geology. https://doi.org/10.1130/G51355.1
Higgins, O., Sheldrake, T., Caricchi, L., 2021a. Machine learning thermobarometry and chemometry using amphibole and clinopyroxene: a window into the roots of an arc volcano (Mount Liamuiga, Saint Kitts). Contrib Mineral Petrol 177, 10. https://doi.org/10.1007/s00410-021-01874-6
Higgins, O., Sheldrake, T., Caricchi, L., 2021b. Quantitative chemical mapping of plagioclase as a tool for the interpretation of volcanic stratigraphy: an example from Saint Kitts, Lesser Antilles. Bull Volcanol 83, 51. https://doi.org/10.1007/s00445-021-01476-x
Hirschmann, M.M., Ghiorso, M.S., Davis, F.A., Gordon, S.M., Mukherjee, S., Grove, T.L., Krawczynski, M., Medard, E., Till, C.B., 2008. Library of Experimental Phase Relations (LEPR): A database and Web portal for experimental magmatic phase equilibria data. Geochemistry, Geophysics, Geosystems 9. https://doi.org/10.1029/2007GC001894
Husen, A., Almeev, R.R., Holtz, F., 2016. The Effect of H2O and Pressure on Multiple Saturation and Liquid Lines of Descent in Basalt from the Shatsky Rise. Journal of Petrology 57, 309–344. https://doi.org/10.1093/petrology/egw008
Irvine, T.N., Baragar, W.R.A., 1971. A Guide to the Chemical Classification of the Common Volcanic Rocks. Can. J. Earth Sci. 8, 523–548. https://doi.org/10.1139/e71-055
Jackson, M.D., Blundy, J., Sparks, R.S.J., 2018. Chemical differentiation, cold storage and remobilization of magma in the Earth's crust. Nature 564, 405–409. https://doi.org/10.1038/s41586-018-0746-2
Jenkins, J., Maclennan, J., Green, R.G., Cottaar, S., Deuss, A.F., White, R.S., 2018. Crustal Formation on a Spreading Ridge Above a Mantle Plume: Receiver Function Imaging of the Icelandic Crust. Journal of Geophysical Research: Solid Earth 123, 5190–5208. https://doi.org/10.1029/2017JB015121
Jorgenson, C., Caricchi, L., Chiaradia, M., Ágreda-López, M., Giordano, G., 2024. Rapid accumulation and ascent precedes caldera forming eruption of low viscosity magma. Contrib Mineral Petrol 179, 16. https://doi.org/10.1007/s00410-023-02091-z
Jorgenson, C., Higgins, O., Petrelli, M., Bégué, F., Caricchi, L., 2022. A Machine Learning-Based Approach to Clinopyroxene Thermobarometry: Model Optimization and Distribution for Use in Earth Sciences. Journal of Geophysical Research: Solid Earth 127, e2021JB022904. https://doi.org/10.1029/2021JB022904

Kelley, D.F., Barton, M., 2008. Pressures of Crystallization of Icelandic Magmas. Journal of Petrology 49, 465–492. https://doi.org/10.1093/petrology/egm089
Kent, A.J.R., Darr, C., Koleszar, A.M., Salisbury, M.J., Cooper, K.M., 2010. Preferential eruption of andesitic magmas through recharge filtering. Nature Geosci 3, 631–636. https://doi.org/10.1038/ngeo924
Libourel, G., Boivin, P., Biggar, G.M., 1989. The univariant curve liquid = forsterite + anorthite + diopside in the system CMAS at 1 bar: solid solutions and melt structure. Contr. Mineral. and Petrol. 102, 406–421. https://doi.org/10.1007/BF00371084
Lissenberg, C.J., MacLeod, C.J., Bennett, E.N., 2019. Consequences of a crystal mush-dominated magma plumbing system: a mid-ocean ridge perspective. Philosophical Transactions of the Royal Society A: Mathematical, Physical and Engineering Sciences 377, 20180014. https://doi.org/10.1098/rsta.2018.0014
Longpré, M.-A., Klügel, A., Diehl, A., Stix, J., 2014. Mixing in mantle magma reservoirs prior to and during the 2011–2012 eruption at El Hierro, Canary Islands. Geology 42, 315–318. https://doi.org/10.1130/G35165.1
Maclennan, J., MKenzie, D., Gronvöld, K., Slater, L., 2001. Crustal accretion under northern Iceland. Earth and Planetary Science Letters 191, 295–310. https://doi.org/10.1016/S0012-821X(01)00420-4
Magee, C., Stevenson, C.T.E., Ebmeier, S.K., Keir, D., Hammond, J.O.S., Gottsmann, J.H., Whaler, K.A., Schofield, N., Jackson, C.A.-L., Petronis, M.S., O'Driscoll, B., Morgan, J., Cruden, A., Vollgger, S.A., Dering, G., Micklethwaite, S., Jackson, M.D., 2018. Magma Plumbing Systems: A Geophysical Perspective. Journal of Petrology 59, 1217–1251. https://doi.org/10.1093/petrology/egy064
Magee, R., Ubide, T., Kahl, M., 2020. The Lead-up to Mount Etna's Most Destructive Historic Eruption (1669). Cryptic Recharge Recorded in Clinopyroxene. Journal of Petrology 61, egaa025. https://doi.org/10.1093/petrology/egaa025
Masotta, M., Mollo, S., Freda, C., Gaeta, M., Moore, G., 2013. Clinopyroxene–liquid thermometers and barometers specific to alkaline differentiated magmas. Contrib Mineral Petrol 166, 1545–1561. https://doi.org/10.1007/s00410-013-0927-9
Meen, J.K., 1990. Elevation of potassium content of basaltic magma by fractional crystallization: the effect of pressure. Contr. Mineral. and Petrol. 104, 309–331. https://doi.org/10.1007/BF00321487
Michael, P., 1995. Regionally distinctive sources of depleted MORB: Evidence from trace elements and H2O. Earth and Planetary Science Letters 131, 301–320. https://doi.org/10.1016/0012-821X(95)00023-6
Michael, P.J., Cornell, W.C., 1998. Influence of spreading rate and magma supply on crystallization and assimilation beneath mid-ocean ridges: Evidence from chlorine and major element chemistry of mid-ocean ridge basalts. Journal of Geophysical Research: Solid Earth 103, 18325–18356. https://doi.org/10.1029/98JB00791
Mollo, S., Del Gaudio, P., Ventura, G., Iezzi, G., Scarlato, P., 2010. Dependence of clinopyroxene composition on cooling rate in basaltic magmas: Implications for thermobarometry. Lithos 118, 302–312. https://doi.org/10.1016/j.lithos.2010.05.006
Neave, D.A., Buisman, I., Maclennan, J., 2017. Continuous mush disaggregation during the long-lasting Laki fissure eruption, Iceland. American Mineralogist 102, 2007–2021. https://doi.org/10.2138/am-2017-6015CCBY

Neave, D.A., Maclennan, J., Hartley, M.E., Edmonds, M., Thordarson, T., 2014. Crystal Storage and Transfer in Basaltic Systems: the Skuggafjöll Eruption, Iceland. Journal of Petrology 55, 2311–2346. https://doi.org/10.1093/petrology/egu058

Neave, D.A., Namur, O., 2022. Plagioclase archives of depleted melts in the oceanic crust. Geology. https://doi.org/10.1130/G49840.1

Neave, D.A., Namur, O., Shorttle, O., Holtz, F., 2019. Magmatic evolution biases basaltic records of mantle chemistry towards melts from recycled sources. Earth and Planetary Science Letters 520, 199–211. https://doi.org/10.1016/j.epsl.2019.06.003

Neave, D.A., Putirka, K.D., 2017. A new clinopyroxene-liquid barometer, and implications for magma storage pressures under Icelandic rift zones. American Mineralogist 102, 777–794. https://doi.org/10.2138/am-2017-5968

Passmore, E., Maclennan, J., Fitton, G., Thordarson, T., 2012. Mush Disaggregation in Basaltic Magma Chambers: Evidence from the ad 1783 Laki Eruption. Journal of Petrology 53, 2593–2623. https://doi.org/10.1093/petrology/egs061

Pedersen, G.B.M., Höskuldsson, A., Dürig, T., Thordarson, T., Jónsdóttir, I., Riishuus, M.S., Óskarsson, B.V., Dumont, S., Magnusson, E., Gudmundsson, M.T., Sigmundsson, F., Drouin, V.J.P.B., Gallagher, C., Askew, R., Gudnason, J., Moreland, W.M., Nikkola, P., Reynolds, H.I., Schmith, J., 2017. Lava field evolution and emplacement dynamics of the 2014–2015 basaltic fissure eruption at Holuhraun, Iceland. Journal of Volcanology and Geothermal Research 340, 155–169. https://doi.org/10.1016/j.jvolgeores.2017.02.027

Petrelli, M., Caricchi, L., Perugini, D., 2020. Machine Learning Thermo-Barometry: Application to Clinopyroxene-Bearing Magmas. Journal of Geophysical Research: Solid Earth 125, e2020JB020130. https://doi.org/10.1029/2020JB020130

Piñeiro, G., Perelman, S., Guerschman, J.P., Paruelo, J.M., 2008. How to evaluate models: Observed vs. predicted or predicted vs. observed? Ecological Modelling 216, 316–322. https://doi.org/10.1016/j.ecolmodel.2008.05.006

Popa, R.-G., Bachmann, O., Huber, C., 2021. Explosive or effusive style of volcanic eruption determined by magma storage conditions. Nat. Geosci. 14, 781–786. https://doi.org/10.1038/s41561-021-00827-9

Presnall, D.C., Dixon, S.A., Dixon, J.R., O'Donnell, T.H., Brenner, N.L., Schrock, R.L., Dycus, D.W., 1978. Liquidus phase relations on the join diopside-forsterite-anorthite from 1 atm to 20 kbar: Their bearing on the generation and crystallization of basaltic magma. Contr. Mineral. and Petrol. 66, 203–220. https://doi.org/10.1007/BF00372159

Putirka, K., 2016. Amphibole thermometers and barometers for igneous systems and some implications for eruption mechanisms of felsic magmas at arc volcanoes. American Mineralogist 101, 841–858. https://doi.org/10.2138/am-2016-5506

Putirka, K., 1997. Magma transport at Hawaii: Inferences based on igneous thermobarometry. Geology 25, 69–72. https://doi.org/10.1130/0091-7613(1997)025<0069:MTAHIB>2.3.CO;2

Putirka, K.D., 2008. Thermometers and Barometers for Volcanic Systems. Reviews in Mineralogy and Geochemistry 69, 61–120. https://doi.org/10.2138/rmg.2008.69.3

R Core Team, 2023. R: A Language and Environment for Statistical Computing.

Re, G., Corsaro, R.A., D'Oriano, C., Pompilio, M., 2021. Petrological monitoring of active volcanoes: A review of existing procedures to achieve best practices and operative

protocols during eruptions. Journal of Volcanology and Geothermal Research 419, 107365. https://doi.org/10.1016/j.jvolgeores.2021.107365
Ridolfi, F., Renzulli, A., 2012. Calcic amphiboles in calc-alkaline and alkaline magmas: thermobarometric and chemometric empirical equations valid up to 1,130° C and 2.2 GPa. Contributions to Mineralogy and Petrology 163, 877–895. https://doi.org/10.1007/s00410-011-0704-6
Saunders, K., Blundy, J., Dohmen, R., Cashman, K., 2012. Linking Petrology and Seismology at an Active Volcano. Science 336, 1023–1027. https://doi.org/10.1126/science.1220066
Sheldrake, T., Higgins, O., 2021. Classification, segmentation and correlation of zoned minerals. Computers & Geosciences 156, 104876. https://doi.org/10.1016/j.cageo.2021.104876
Shi, P., 1993. Low-Pressure Phase Relationships in the System Na2O—CaO—FeO—MgO—Al2O3—SiO2 at 1100°C, with Implications for the Differentiation of Basaltic Magmas. Journal of Petrology 34, 743–762. https://doi.org/10.1093/petrology/34.4.743
Shi, P., 1992. Basalt evolution at low pressure: implications from an experimental study in the system CaO-FeO-MgO-Al2O3-SiO2. Contr. Mineral. and Petrol. 110, 139–153. https://doi.org/10.1007/BF00310735
Sigmundsson, F., Hooper, A., Hreinsdóttir, S., Vogfjörd, K.S., Ófeigsson, B.G., Heimisson, E.R., Dumont, S., Parks, M., Spaans, K., Gudmundsson, G.B., Drouin, V., Árnadóttir, T., Jónsdóttir, K., Gudmundsson, M.T., Högnadóttir, T., Fridriksdóttir, H.M., Hensch, M., Einarsson, P., Magnússon, E., Samsonov, S., Brandsdóttir, B., White, R.S., Ágústsdóttir, T., Greenfield, T., Green, R.G., Hjartardóttir, Á.R., Pedersen, R., Bennett, R.A., Geirsson, H., La Femina, P.C., Björnsson, H., Pálsson, F., Sturkell, E., Bean, C.J., Möllhoff, M., Braiden, A.K., Eibl, E.P.S., 2015. Segmented lateral dyke growth in a rifting event at Bárðarbunga volcanic system, Iceland. Nature 517, 191–195. https://doi.org/10.1038/nature14111
Sisson, T.W., Grove, T.L., 1993. Experimental investigations of the role of H2O in calc-alkaline differentiation and subduction zone magmatism. Contr. Mineral. and Petrol. 113, 143–166. https://doi.org/10.1007/BF00283225
Smithies, S.L., Harmon, L.J., Allen, S.M., Gravley, D.M., Gualda, G.A.R., 2023. Following magma: The pathway of silicic magmas from extraction to storage during an ignimbrite flare-up, Taupō Volcanic Zone, New Zealand. Earth and Planetary Science Letters 607, 118053. https://doi.org/10.1016/j.epsl.2023.118053
Sobolev, A.V., Chaussidon, M., 1996. H2O concentrations in primary melts from supra-subduction zones and mid-ocean ridges: Implications for H2O storage and recycling in the mantle. Earth and Planetary Science Letters 137, 45–55. https://doi.org/10.1016/0012-821X(95)00203-O
Solano, J.M.S., Jackson, M.D., Sparks, R.S.J., Blundy, J., 2014. Evolution of major and trace element composition during melt migration through crystalline mush: Implications for chemical differentiation in the crust. American Journal of Science 314, 895–939. https://doi.org/10.2475/05.2014.01
Stock, M.J., Bagnardi, M., Neave, D.A., Maclennan, J., Bernard, B., Buisman, I., Gleeson, M.L.M., Geist, D., 2018. Integrated Petrological and Geophysical Constraints on Magma System Architecture in the Western Galápagos Archipelago: Insights From Wolf Volcano. Geochemistry, Geophysics, Geosystems 19, 4722–4743. https://doi.org/10.1029/2018GC007936

Stock, M.J., Geist, D., Neave, D.A., Gleeson, M.L.M., Bernard, B., Howard, K.A., Buisman, I., Maclennan, J., 2020. Cryptic evolved melts beneath monotonous basaltic shield volcanoes in the Galápagos Archipelago. Nature Communications 11, 3767. https://doi.org/10.1038/s41467-020-17590-x

Ubide, T., Márquez, Á., Ancochea, E., Huertas, M.J., Herrera, R., Coello-Bravo, J.J., Sanz-Mangas, D., Mulder, J., MacDonald, A., Galindo, I., 2023. Discrete magma injections drive the 2021 La Palma eruption. Science Advances 9, eadg4813. https://doi.org/10.1126/sciadv.adg4813

Voigt, M., Coogan, L.A., von der Handt, A., 2017. Experimental investigation of the stability of clinopyroxene in mid-ocean ridge basalts: The role of Cr and Ca/Al. Lithos 274–275, 240–253. https://doi.org/10.1016/j.lithos.2017.01.003

Wallace, P.J., 2005. Volatiles in subduction zone magmas: concentrations and fluxes based on melt inclusion and volcanic gas data. Journal of Volcanology and Geothermal Research 140, 217–240.

Weber, G., Blundy, J., 2023. A machine learning-based thermometer, barometer and hygrometer for magmatic liquids.

Weber, G., Caricchi, L., Arce, J.L., 2020. The Long-Term Life-Cycle of Nevado de Toluca Volcano (Mexico): Insights Into the Origin of Petrologic Modes. Frontiers in Earth Science 8.

Wilke, S., Holtz, F., Neave, D.A., Almeev, R., 2017. The Effect of Anorthite Content and Water on Quartz–Feldspar Cotectic Compositions in the Rhyolitic System and Implications for Geobarometry. Journal of Petrology 58, 789–818. https://doi.org/10.1093/petrology/egx034

Yang, H.-J., Kinzler, R.J., Grove, T.L., 1996. Experiments and models of anhydrous, basaltic olivine-plagioclase-augite saturated melts from 0.001 to 10 kbar. Contrib Mineral Petrol 124, 1–18. https://doi.org/10.1007/s004100050169

Yoder, H.S., 1965. Diopside-anorthite-water at five and ten kilobars and its bearing on explosive volcanism. Carnegie Institution of Washington Yearbook 64, 82–89.

Ziberna, L., Green, E.C.R., Blundy, J.D., 2017. Multiple-reaction geobarometry for olivine-bearing igneous rocks. American Mineralogist 102, 2349–2366. https://doi.org/10.2138/am-2017-6154

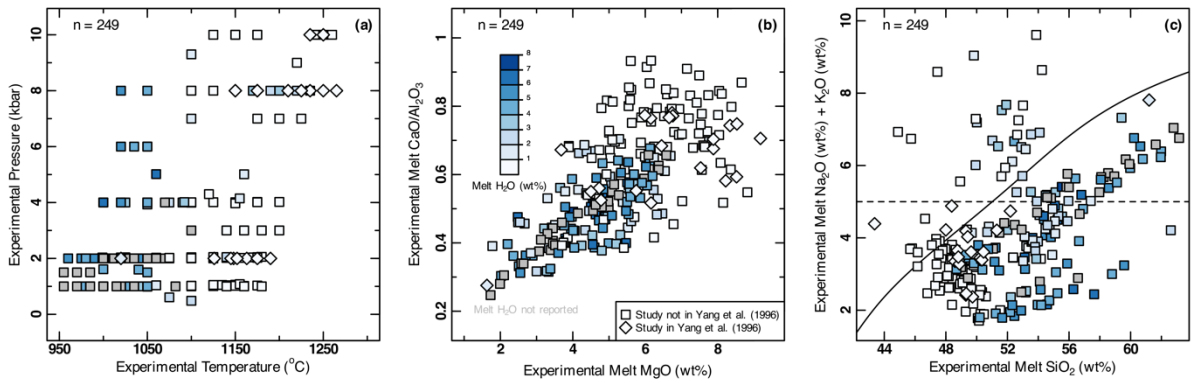

Fig.1: (**a**) Temperature (˚C) versus pressure (kbar); (**b**) melt MgO (wt%) versus melt CaO/Al_2O_3; and (**c**) melt SiO_2 (wt%) versus melt Na_2O+K_2O (wt%) for $OPAM_{SAT}$ equilibrium experiments, colour contoured for melt H_2O (wt%). Grey symbols are hydrous experiments for which a H_2O content is not reported. Diamonds are experiments from studies used to calibrate the Yang et al (1996) cotectic equations. The black curvilinear boundary in (c) is the alkaline-subalkaline transition boundary (Irvine and Baragar, 1971). Melt compositions are normalised to 100 wt% anhydrous with all Fe as FeO.

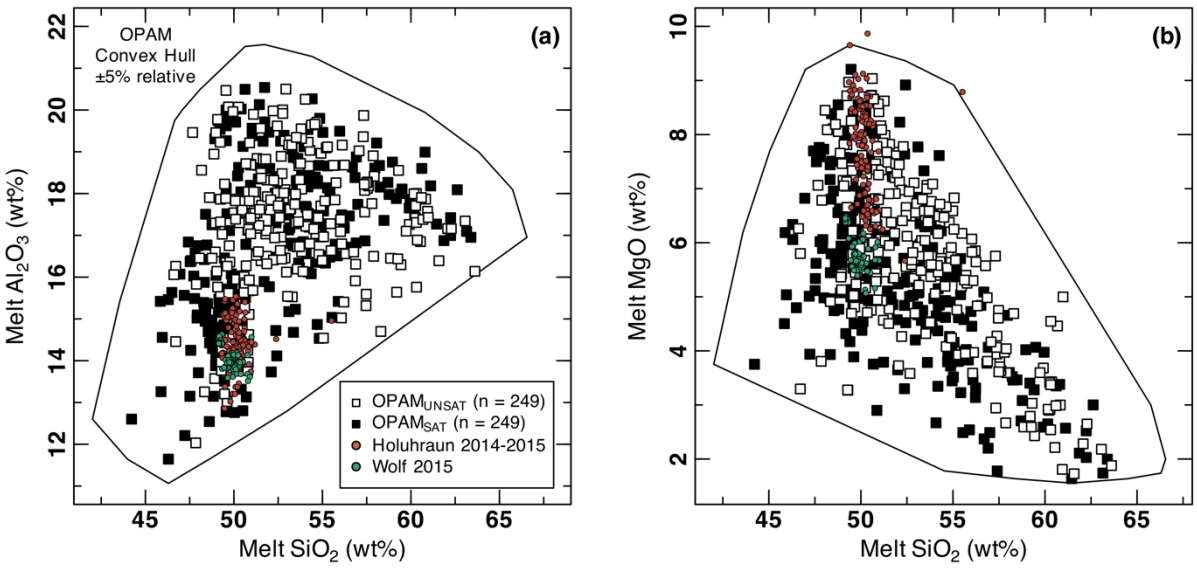

Fig. 2: (**a**) Melt SiO_2 (wt%) versus melt Al_2O_3 (wt%); and (**b**) melt SiO_2 (wt%) versus melt MgO (wt%) for $OPAM_{SAT}$ and $OPAM_{UNSAT}$. $OPAM_{SAT}$ experiments were compiled for this study and are presented in Supplementary Table 1a. $OPAM_{UNSAT}$ experiments (olivine ±

plagioclase ± augitic clinopyroxene ±Fe-oxides) are from the compilation of Weber and Blundy (2023; Supplementary Table 2a). The OPAM convex hull is a polygon connecting the outermost OPAM-saturated points in X-Y space with ±5% relative added to account for analytical uncertainty (black field in both figures). Melts from the 2015 eruption of Wolf Volcano (Galápagos; Stock et al., 2018, 2020) and the 2014-2015 Holuhraun eruption (Iceland; Hartley et al., 2018) are also plotted (see Discussion; Supplementary Table 5). All experimental and natural melt compositions are plotted normalised to the 8 critical oxides used for the OPAM saturation test.

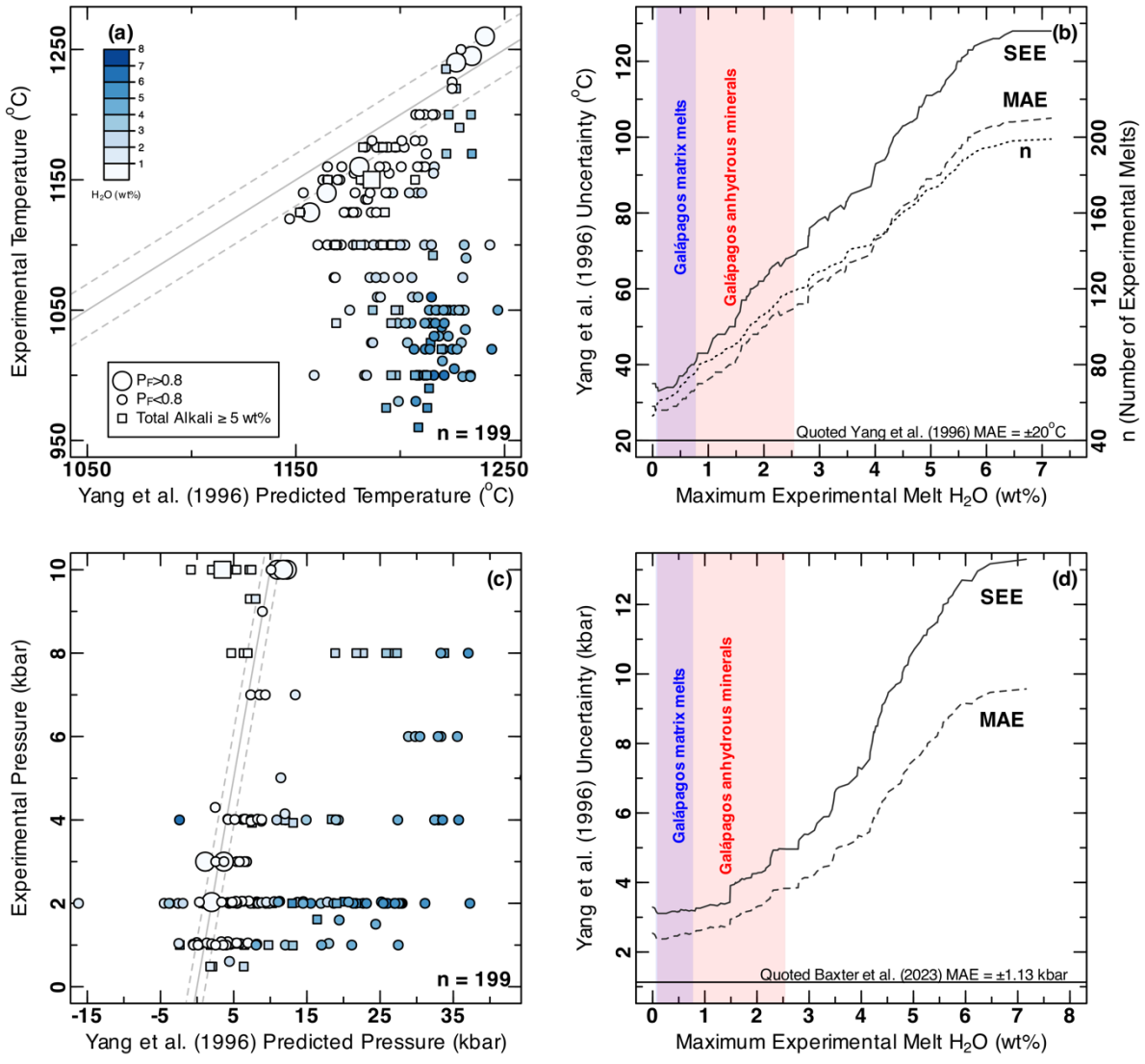

Fig. 3: Performance of the Yang et al (1996) thermometer and barometer for an independent test of 199 $OPAM_{SAT}$ experiments from studies not used in the original Yang et al (1996)

calibration. (**a**) The predicted temperature (˚C) versus experimental temperature (˚C). (**b**) The SEE and MAE for temperature (˚C) as a function of melt H_2O (wt%). The line for n shows the number of experiments with the corresponding melt H_2O content on the x axis or less used to calculate the SEE or MAE. (**c**) The predicted pressure (kbar) versus experimental pressure (kbar). (**d**) The SEE and MAE for pressure (kbar) as a function of melt H_2O (wt%). In (a) and (c) points are colour coded for melt H_2O (wt%) and large symbols indicate experiments which pass the statistical filter of Hartley et al (2018) with a $P_F \geq 0.8$ (see text for details). Solid line is 1:1 and dashed lines are the bounds of the quoted uncertainty for the Yang et al (1996) thermometer (±20 ˚C) and barometer (±1.13 kbar) respectively. In (b) and (d) the ranges of H_2O (wt%) measured for Galápagos melts and calculated from nominally anhydrous minerals are shown (Gleeson et al., 2021).

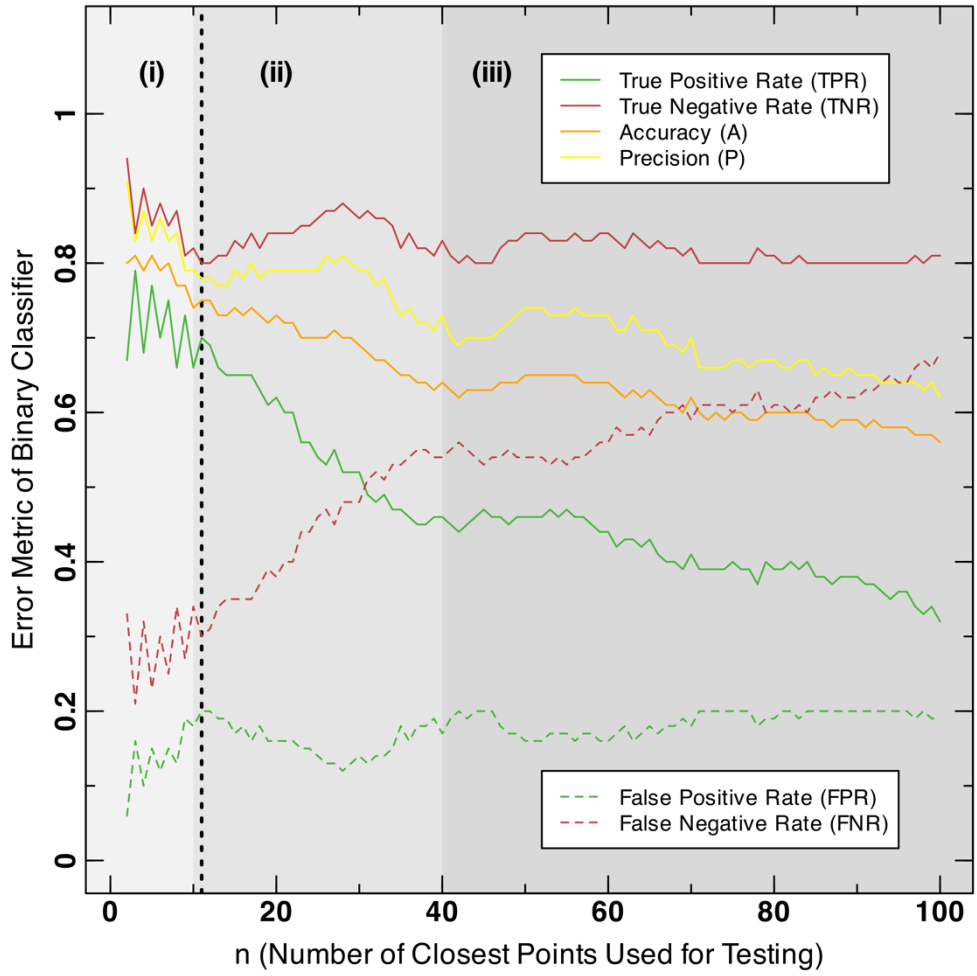

Fig. 4: Performance (Equation 9a-9f) of our statistical test for $OPAM_{SAT}$ melts as a function of n (the number of adjacent experiments considered in multidimensional space when testing if a natural melt is $OPAM_{SAT}$). Grey boxes (i, ii, iii) highlight changes in test performance as a function of n and are discussed in text. The chosen n used for our statistical test is 11 (thick dashed line) at the start of region (ii).

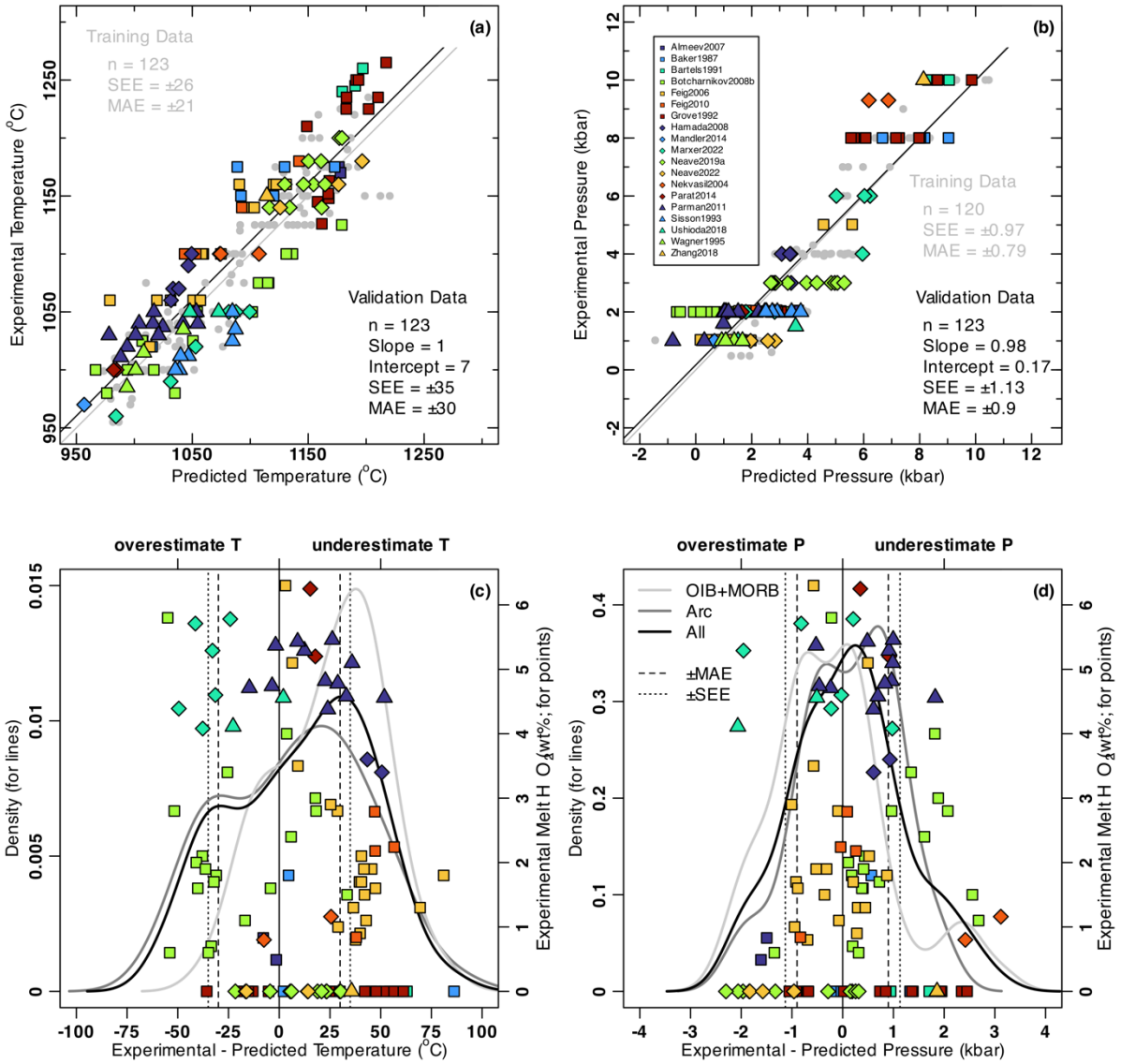

Fig. 5: The performance of our new OPAM thermobarometer using the compiled training and validation data (Supplementary Table 1a). (**a**) Experimental temperature (˚C) versus predicted temperature (˚C). (**b**) Experimental pressure (kbar) versus predicted pressure (kbar). (**c**) Experimental temperature (˚C) minus predicted temperature (˚C) and (**d**) experimental pressure (kbar) minus predicted pressure (kbar) as a function of classified geodynamic setting (lines) and experimental melt H_2O (wt%; points). In (a) and (b) summary statistics for training (grey points) and validation (coloured points) datasets are provided in the plot area. Grey solid line is the 1:1 line, black dashed lines are the bounds of the quoted validation SEE, and the black

solid line is a linear fit between predicted (x) and experimental (y) values. In (c) and (d) geodynamic settings for experimental studies are either arc or ocean island basalt (OIB) plus mid-ocean ridge basalt (MORB).

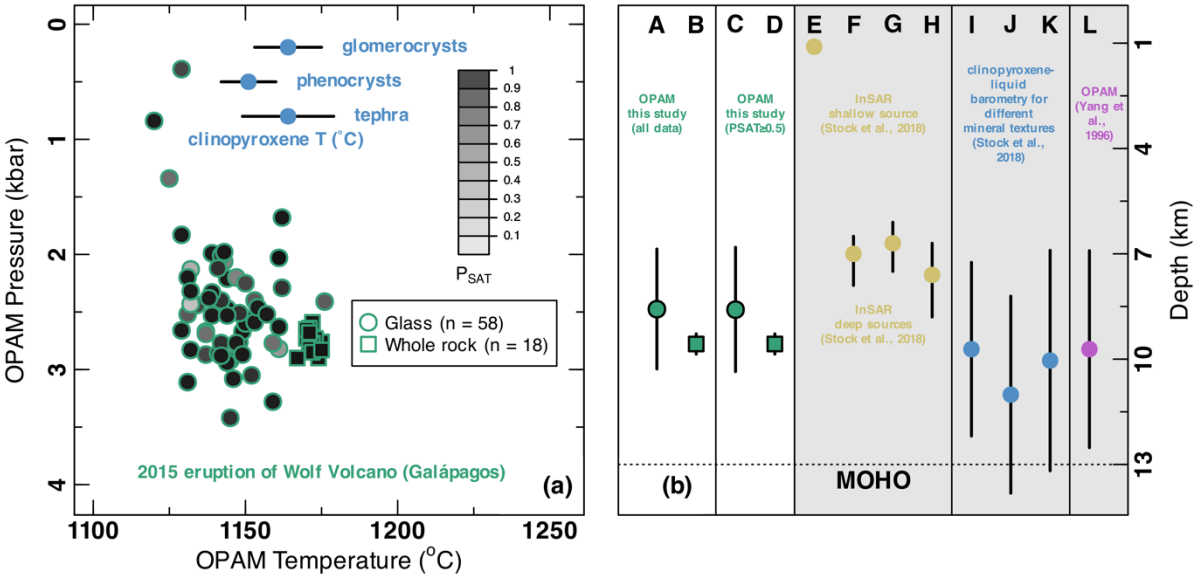

Fig. 6: (**a**) Pressure (kbar) versus temperature (˚C) using our new OPAM thermobarometer for all matrix glass and whole rock data from the 2015 eruption of Wolf Volcano (Galápagos; Stock et al., 2018). Data points are colour contoured for P_{SAT} using our binary classifier for $OPAM_{SAT}$ melts. Clinopyroxene *T* for the three textural subclasses of clinopyroxene from Stock et al., (2018) are shown as mean±1σ ranges for comparison. (**b**) *P* converted to depth using Equation 11 for petrological and geophysical methods discussed in text, with letters corresponding as follows: A = mean±1σ of all matrix glass values using Equation 10a; B = mean±1σ of all whole rock values using Equation 10a; C = mean±1σ of matrix glass values with P_{SAT}≥0.5 using Equation 10a; D = mean±1σ of whole rock values with P_{SAT}≥0.5 using Equation 10a; E = pre-eruptive shallow source from Stock et al., (2018) using InSAR; F, G, H = syn-eruptive deep source of the circumferential fissure phase, caldera fill phase, and the entire eruption, respectively, from Stock et al., (2018) using InSAR; I, J, K = clinopyroxene-liquid barometry (Neave and Putirka, 2017) for glomerocrystic, phenocrystic, and tephra-hosted

clinopyroxene, respectively, from Stock et al., (2018). The Moho depth is shown by the dashed line (Feighner and Richards, 1994).

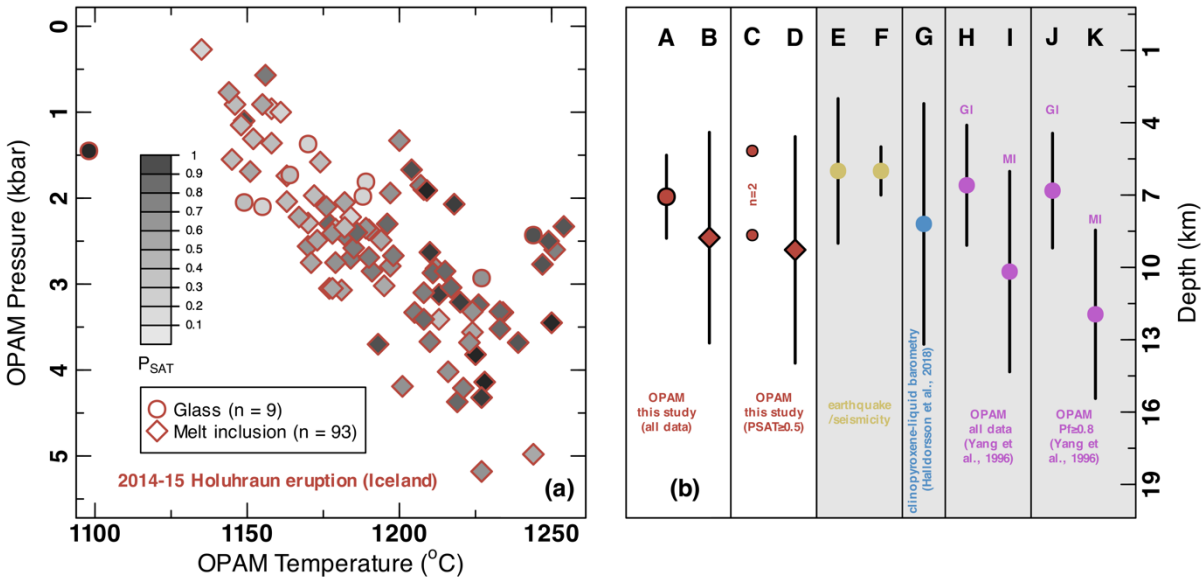

Fig. 7: (**a**) Pressure (kbar) versus temperature (˚C) using our new OPAM thermobarometer for all matrix glass and melt inclusion data from the 2014-2015 Holuhraun eruption (Iceland; Hartley et al., 2018). Data points are colour contoured for P_{SAT} using our binary classifier for $OPAM_{SAT}$ melts. (**b**) *P* converted to depth using a fixed density of $2.86*10^6$ kg/m^3 for petrological and geophysical methods discussed in text, with letters corresponding as follows: A = mean±1σ of all matrix glass values using Equation 10a; B = mean±1σ of all melt inclusion values using Equation 10a; C = mean±1σ of matrix glass values with $P_{SAT}\geq0.5$ using Equation 10a; D = mean±1σ of melt inclusion values with $P_{SAT}\geq0.5$ using Equation 10a; E = pre-eruptive seismicity (Sigmundsson et al., 2015); F = most common earthquake hypocentral depth (Ágústsdóttir et al., 2016); G = clinopyroxene-liquid barometry (Neave and Putirka, 2017) for clinopyroxene crystals screened for textural equilibrium (Halldórsson et al., (2018); H, I = OPAM barometry of glass and melt inclusions respectively using the Yang et al (1996) equations implemented by the approach of Hartley et al (2018); J, K = as for H and I but with data filtered for $P_f\geq0.8$ according to the saturation test of Hartley et al (2018).